

Journal of Geophysical Research: Planets

RESEARCH ARTICLE

10.1002/2013JE004580

Key Points:

- Spatially resolved near-global Hapke parameter maps were derived from LROC WAC
- Photometric properties of the lunar surface vary with wavelength and composition
- Highland is more backscattering relative to maria

Correspondence to:
H. Sato,
hsato@ser.asu.edu**Citation:**
Sato, H., M. S. Robinson, B. Hapke, B. W. Denevi, and A. K. Boyd (2014), Resolved Hapke parameter maps of the Moon, *J. Geophys. Res. Planets*, 119, 1775–1805, doi:10.1002/2013JE004580.

Received 27 NOV 2013

Accepted 27 JUN 2014

Accepted article online 1 JUL 2014

Published online 8 AUG 2014

Resolved Hapke parameter maps of the Moon

H. Sato¹, M. S. Robinson¹, B. Hapke², B. W. Denevi³, and A. K. Boyd¹¹School of Earth and Space Exploration, Arizona State University, Tempe, Arizona, USA, ²Department of Geology and Planetary Science, University of Pittsburgh, Pittsburgh, Pennsylvania, USA, ³Johns Hopkins University Applied Physics Laboratory, Laurel, Maryland, USA

Abstract We derived spatially resolved near-global Hapke photometric parameter maps of the Moon from 21 months of Lunar Reconnaissance Orbiter Camera (LROC) Wide Angle Camera (WAC) multispectral observations using a novel “tile-by-tile method” (1° latitude by 1° longitude bins). The derived six parameters (w, b, c, B_{S0}, h_s , and $\bar{\theta}_p$) for each tile were used to normalize the observed reflectance (standard angles $i = g = 60^{\circ}$, $e = 0^{\circ}$ instead of the traditional angles $i = g = 30^{\circ}$, $e = 0^{\circ}$) within each tile, resulting in accurate normalization optimized for the local photometric response. Each pixel in the seven-color near-global mosaic (70° S to 70° N and 0° E to 360° E) was computed by the median of normalized reflectance from large numbers of repeated observations (UV: \sim 50 and visible: \sim 126 on average). The derived mosaic exhibits no significant artifacts with latitude or along the tile boundaries, demonstrating the quality of the normalization procedure. The derived Hapke parameter maps reveal regional photometric response variations across the lunar surface. The b, c (Henyey-Greenstein double-lobed phase function parameters) maps demonstrate decreased backscattering in the maria relative to the highlands (except 321 nm band), probably due to the higher content of both SMFe (submicron iron) and ilmenite in the interiors of back scattering agglutinates in the maria. The h_s (angular width of shadow hiding opposition effect) map exhibits relatively lower values in the maria than the highlands and slightly higher values for immature highland crater ejecta, possibly related to the variation in a grain size distribution of regolith.

1. Introduction

Photometric normalization is a technique to adjust scene brightness such that each location on the surface appears as if illuminated and viewed from the same angles and is particularly useful for the analysis of planetary image data sets. In the particular case of the Lunar Reconnaissance Orbiter Camera (LROC) Wide Angle Camera (WAC), a global data set is acquired over a lunar rotation period (27.3 days) through pole-to-pole imaging sequences achieved 12.7 times per 24 h period [Robinson et al., 2010]. During a single Lunar Reconnaissance Orbiter (LRO) orbit (113 min in 50 km quasi-circular orbit), the Moon rotates 1.03° and the solar incidence angle (measured from the surface normal) at the equator crossing drifts 0.09° . During a monthly WAC global data acquisition period, the solar incidence angle at the equator crossing changes by about 30° . Also, the incidence angle increases poleward within every imaging sequence. The WAC has a 90° field of view (FOV) in monochrome mode (not used in this study) and 60° FOV in seven-color mode (321 to 689 nm) in the cross track direction [Robinson et al., 2010]. Typically, the LRO spacecraft is pointing nadir so the WAC acquires constant low emission angles (angle of camera boresight relative to the surface normal) at the center of the FOV and up to 45° in monochrome mode and up to 30° in seven-color mode at the edges in the cross-track direction. Additionally, due to the push frame design of the WAC, the center of each wavelength filter has a different emission angle (Figure 1). Due to the changes in emission angle within a single frame (cross track, $< 31.3^{\circ}$) and across the filter to filter (down track, $< 7.5^{\circ}$), that also changes the phase angle (angle between camera boresight relative to subsolar vector), the photometric effect on the observed reflectance is significant inside each image. Also, the color differences on the Moon are small, thus true reflectance and color differences from varying points on the surface can only be obtained by accurately normalizing each measurement (pixel) to a common incidence and emission angle.

Numerous normalization schemes can be employed, some are empirical and others are tied to physical properties of the surface. However, obtaining a generalized photometric description of the Moon is not a simple task due to the heterogeneous nature of the lunar surface. The photometric response of geologic materials on the Moon is dominantly a function of mineralogy, grain size, surface roughness, compaction, and state of maturity [McKay et al., 1974; Fischer et al., 1994; Fischer and Pieters, 1996; Lucey et al., 2000]. There

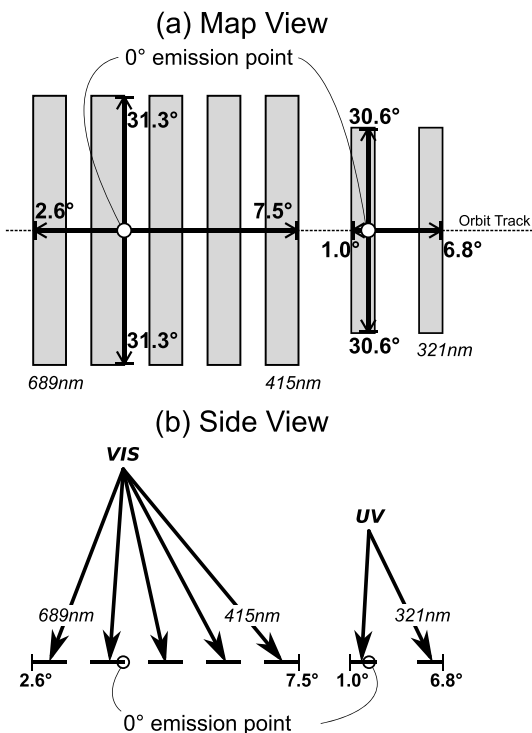


Figure 1. Geometric configuration of two-band UV and five-band visible wavelength frames of the WAC (color mode) in (a) map view and (b) side view. The degree signed value indicates the emission angle at the edge of the field of view. Dashed line indicates the orbit track at the normal observation with threw angle 0° .

a given spot on the Moon, an accurate bidirectional reflectance function can be derived if observations over a significant range of three angle variables (i , e , and g) are available.

Relative to the LROC WAC observations, past spacecraft reflectance measurements of the Moon (Lunar Orbiter, Clementine, Smart-1, Kaguya, Chandrayaan-1) were restricted in the three angle variations due to the steady nadir observations with narrower FOVs and limited repeat observations over a range of

i . Multitemporal Earth-based observations provide repeated reflectance measurements over a range of i , but the variation of e is limited to a few degrees at any given location on the nearside [Kieffer and Wildey, 1996; Kieffer and Stone, 2005; Saiki et al., 2008; Velikodsky et al., 2011].

From 19 September 2009 to 11 December 2011 (Exploration Mission Phase and first part of Science Mission Phase), LRO remained in a 50 km quasi-circular polar orbit [Tooley et al., 2010]. After 11 December 2011, LRO was moved to the current ellipsoidal polar orbit (216 km at north pole, 30 km at south pole, [Folta and Quinn, 2006]). During the 50 km quasi-circular orbit period, the WAC (color mode) typically acquired

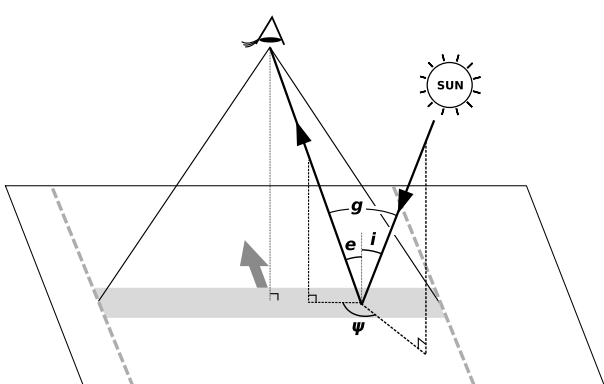


Figure 2. Schematic diagram of incidence (i), emission (e), phase (g), and azimuthal (ψ) angles under the geometric configuration of the WAC. The narrow solid lines indicate the WAC field of view. The foot print of one WAC frame (gray zone), advancing direction (gray arrow), and the widths of single WAC image (gray dashed bold line) along the orbit track are illustrated.

are two major petrologic terrains on the Moon: basaltic mare and anorthositic highlands [McCord et al., 1972; Whitaker, 1972; Pieters and McCord, 1976; Lucey et al., 2006]. Additionally, within each terrain, mineralogy varies as do the grain size distribution and the state of maturity below the 100 m scale of a single WAC pixel [McCord and Johnson, 1970; McCord and Adams, 1973; Hapke, 1973; Hapke et al., 1975; Pieters and McCord, 1976; Pieters, 1977, 1978; Pieters et al., 2000; Lucey et al., 2006].

For over a century the bidirectional reflectance of the Moon has been investigated with laboratory measurements, Earth-based observations, and spacecraft observations. Several models based on both the theoretical and empirical approaches were derived and used with varying levels of success [Minnaert, 1941; Nicodemus, 1965; Akimov, 1975; Wildey, 1963, 1977; McEwen, 1991; Shkuratov et al., 1999; Hillier et al., 1999; Kieffer and Stone, 2005; Hapke et al., 2012; Boyd et al., 2012]. However, due to the spatially variant nature of lunar bidirectional reflectance, a single normalization function applied to a high-resolution global image data set results in locally varying residuals among compositional and maturity units. Since reflectance is controlled and described by three basic geometric angles: incidence (i), emission (e), and phase (g) angles (Figure 2) for

about 40 to 81 km (1.3° to 3.1° at the equator) cross-orbit segments for each orbit, which result in greater than 50% cross-track overlap between neighboring orbits at the equator. Note that with the WAC FOV (60°), the ground coverage of each image changes with the spacecraft altitude from the lunar surface, and the altitude of LRO drifts between 37 and 70 km due to the irregular lunar gravity field and topography. From the 50 km orbit period, each month the WAC achieved near-global coverage with unique set of viewing and illumination geometries for any given location on the Moon, with a 100 m pixel scale in the visible bands and 400 m pixel scale for the UV bands. There are roughly 27 months of WAC observations (186,299 images excluding night observations) from the 50 km quasi-circular orbits, which theoretically include up to 54 observations for each 100 m location at the equator, and an increasing number of observations at higher latitudes.

These unique multitemporal observations provide significant variation of i , e , and g , from which we derived spatially resolved photometric parameters using Hapke's bidirectional reflectance model [Hapke, 1981, 2002, 2008, 2012a] (hereafter called "Hapke model"). We divided the planet into 1° tiles (30 km scale) and derived Hapke photometric parameters (w , b , c , B_{50} , and h_S , defined below) for each tile using all WAC image pixels geographically belonging to a particular tile. This "tile-by-tile method" reduces uncertainty due to local changes in geologic properties that in turn modify the photometric response of the surface. The spatially independent parameter calculation also allows analysis of regional variations of photometric properties in a geological context.

In this paper we report the results of the photometric normalization of the WAC data set using a novel tile-by-tile method, including a step-by-step description of the parameter calculation scheme and corresponding uncertainty estimates. Finally, from the spatially resolved photometric parameters, we discuss the regional variations of photometric properties of the Moon.

2. Methodology

2.1. Data Preparation

About 66,000 WAC images acquired from February 2010 to October 2011 were used in this study. The observations from September 2009 to January 2010 were incomplete and thus excluded. Also crossover analyzed Spacecraft Position Kernels (SPK) [Mazarico et al., 2011] were available for the observations until October 2011 when we started preparing the WAC data for this study. Only nadir pointing color mode images were included (no monochrome mode). Slewed observations were excluded as they have larger pointing uncertainties. All of the raw image data archived in NASA PDS (Planetary Data System) format (EDR: Experiment Data Record) were decompanded from 8 bit to 12 bit and radiometrically calibrated from raw digital number (DN) value to radiance factor I/F [Hapke, 2012a] according to the procedure described by Robinson et al. [2010]. The i , e , and g angles and the geographic location (latitude: lat and longitude: lon) of each pixel were computed using the crossover analyzed SPK, LRO-derived Camera Kernels (CK), and the GLD100 Digital Terrain Model (DTM) derived from the WAC stereo matching [Scholten et al., 2012]. Historically, i and e angles were computed assuming a spherical Moon due to a paucity of global topographic data sets [e.g., McEwen, 1996; McEwen and Eliason, 1998; Yokota et al., 2011], resulting in significant errors due to uncorrected topographic slopes [Robinson and Jolliff, 2002]. The advent of LRO-based global topographic models (GLD100; 100 m/pix, [Scholten et al., 2012]) represents a key advance in the ability to accurately compute photometric angles for the WAC observations. The radiometric calibration and i , e , g , lat , and lon calculations were achieved by routines in the Integrated Software for Imagers and Spectrometers (ISIS) software developed by the United States Geological Survey (USGS) [Anderson et al., 2004]. The original nadir pixel scale of WAC images (from 50 km altitude) is 384 m for UV bands (321 and 360 nm), and 75 m for visible bands (415, 566, 604, 643, and 689 nm) [Robinson et al., 2010]. The UV bands were processed at their nominal resolution, and the visible bands were resampled to 1/4 scale for samples and 1/2 scale for lines (about 283 m/pixel) to save the data storage resource. These resampling scales are optimized to reduce the original frame size of the visible bands (704 samples by 14 lines) by averaging aliquot numbers of pixels and to minimize the frame size difference between UV (128 samples by 4 lines) and visible bands. All the WAC data processing performed in this study are summarized in Figure 3.

2.2. Photometric Parameter Calculation Procedure

The photometric parameters were derived by model fitting using Hapke model (see section 2.3) against the observed reflectance data (hereafter called fitting data) over the broad range of lighting conditions within

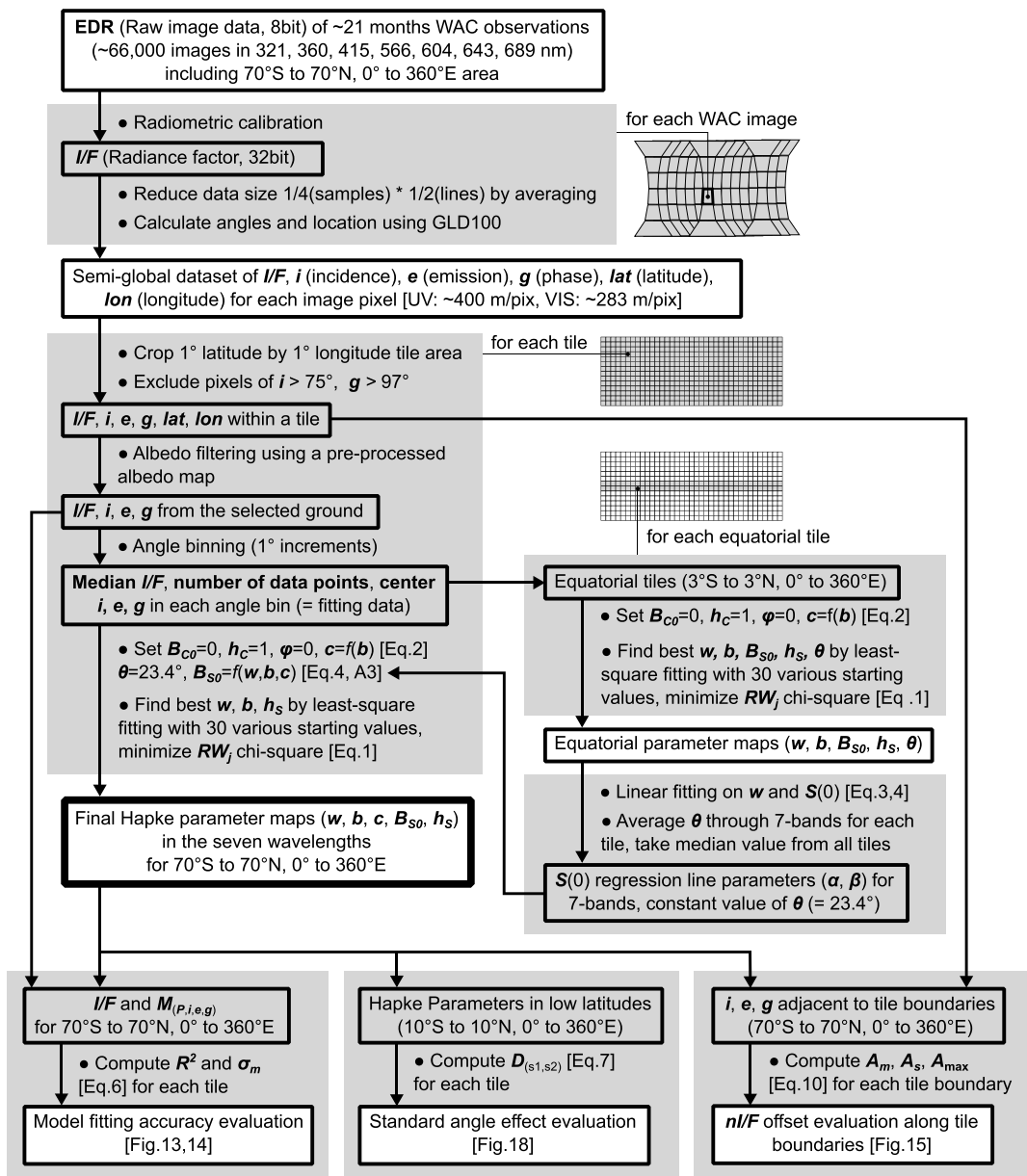


Figure 3. Flow chart of the WAC data processing and the stepwise Hapke parameter calculation performed in this study.

each geographically segmented 1° latitude by 1° longitude tile (referred to simply as “tile”). As the tiles decrease in area toward the poles, the data density per unit area also increases due to orbit convergence. Thus, the number of data points in each tile is comparable at all latitudes. To improve the accuracy of parameter calculation and to save computation time, we reduced the fitting data by “albedo filtering” and “angle binning” (see below).

As shown in the sample tile histogram (Figure 4a), many tiles have multimodal albedo populations, which increase uncertainty in the model fitting for that particular tile (Figure 4b). First, we selected one of the albedo populations (from multimodal spreads) per tile by applying a lower/upper limit threshold. The referenced (relatively rough) albedo values within a tile are supplied by a preprocessed WAC median mosaic (see section 2.4), which was normalized using preexisting parameter maps produced by Sato *et al.* [2011]. The lower/upper limits are given by the range defined as the most frequent albedo value ± 1 standard deviation (dashed lines in Figure 4a) per tile. The resulting subpopulation is typically composed of the dominant and distinct geologic unit within that tile (Figure 4c, unhatched region). The fitting then utilized only the

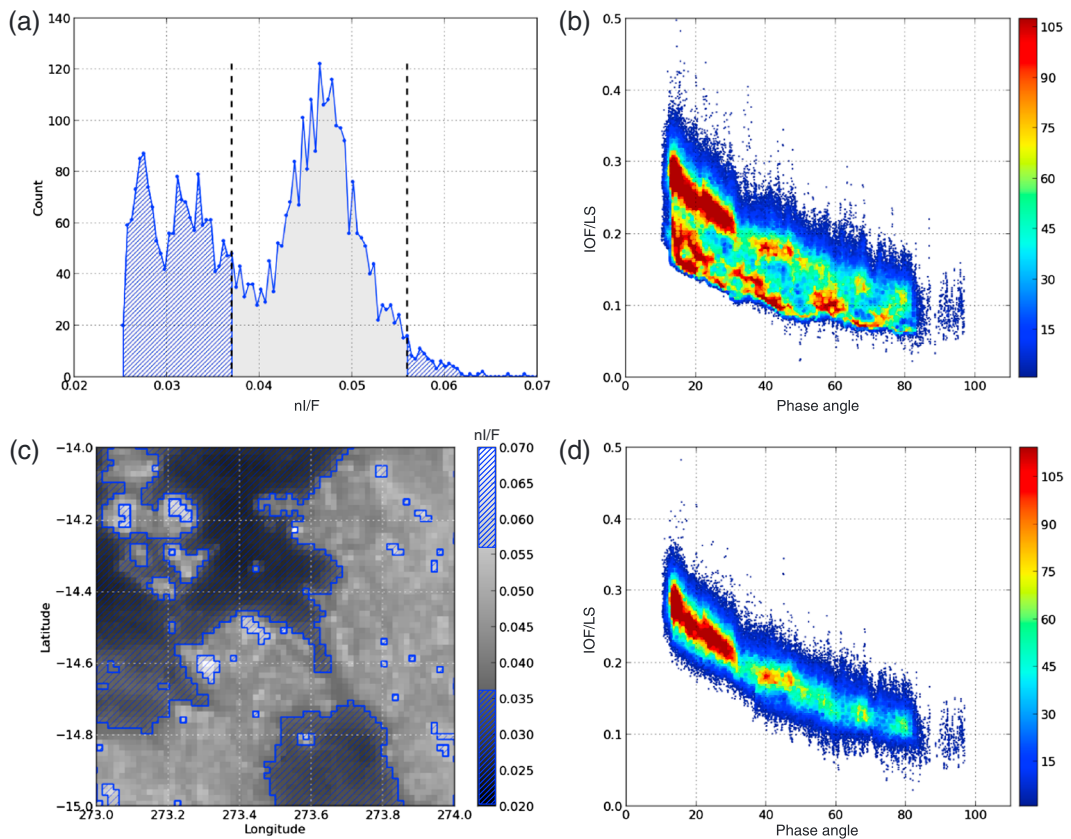


Figure 4. An example of albedo filtering in a tile centered at 14.5°S, 273.5°E, in 643 nm band. (a) The histogram of nl/F from a preprocessed WAC mosaic, (b) density plot of I/F divided by Lommel-Seeliger function ($LS(i, e)$, equation (A2)) versus phase angle g , (c) map view of nl/F from a preprocessed WAC mosaic (1/64° per pixel resolution) in the sample tile, and (d) density plot of I/F divided by $LS(i, e)$ after albedo filtering. The unshaded areas in Figures 4a and 4c correspond to the selected areas after albedo filtering.

reflectance acquired within the dominant unit for the whole tile (Figure 4d). Since many tiles contain more than one discrete albedo unit, this albedo filtering significantly improves the precision of the model fitting.

Next, within each tile the data were binned by the photometric angles i , e , and g to 1° increments, and the median I/F value in each bin was used for fitting. The number of data points in each angle bin was used as an error weight during the fitting (see equation (1)). Since the photometric model is a continuous function and returns one value for each set of i , e , and g angles, this angle binning procedure quickly reaches a more precise solution by reducing the variation of I/F for each set of i , e , and g angles. Compared to the random sampling, this angle binning efficiently reduces background variation of albedo in the data set without losing maximum variations in i , e , and g . The maximum number of bins per tile is 324,000 assuming the ranges of $i = 0^\circ$ to 90° , $e = 0^\circ$ to 30° , and $g = 0^\circ$ to 120° . Due to several factors, however, the actual number of valid bins including data points is typically 2500 to 32,000 which is roughly about 40 times fewer data points before binning. The decreasing range of i for poleward tiles reduces the number of populated bins. The viewing geometry of the WAC with a wide FOV in the cross-track direction but a narrow FOV in the orbit direction (about 2° in visible, 4° in UV at each band, Figure 1a) also contributes to reducing the number of bins. As shown in a sample tile at 30.5°N, 297.5°E (Figures 5a and 5b), the distributions of i , e , and g under this geometry fall on a relatively thin curved surface (Figure 5c) in g , i , and e space, rather than forming a thick cloud. Topographic slopes add scatter in this distribution and increase the number of populated bins, which are still significantly smaller than the data points before binning.

The minimum and maximum incidence angles within a tile depend on latitude and the variation in beta angle (the angle between the orbit plane of the spacecraft and the sun vector) within the tile. Since the beta angle cycles throughout a year and shifts relative to longitude, every spot on the surface is observed under different beta angles (and thus incidence angles) from month to month. In our data set, minimum

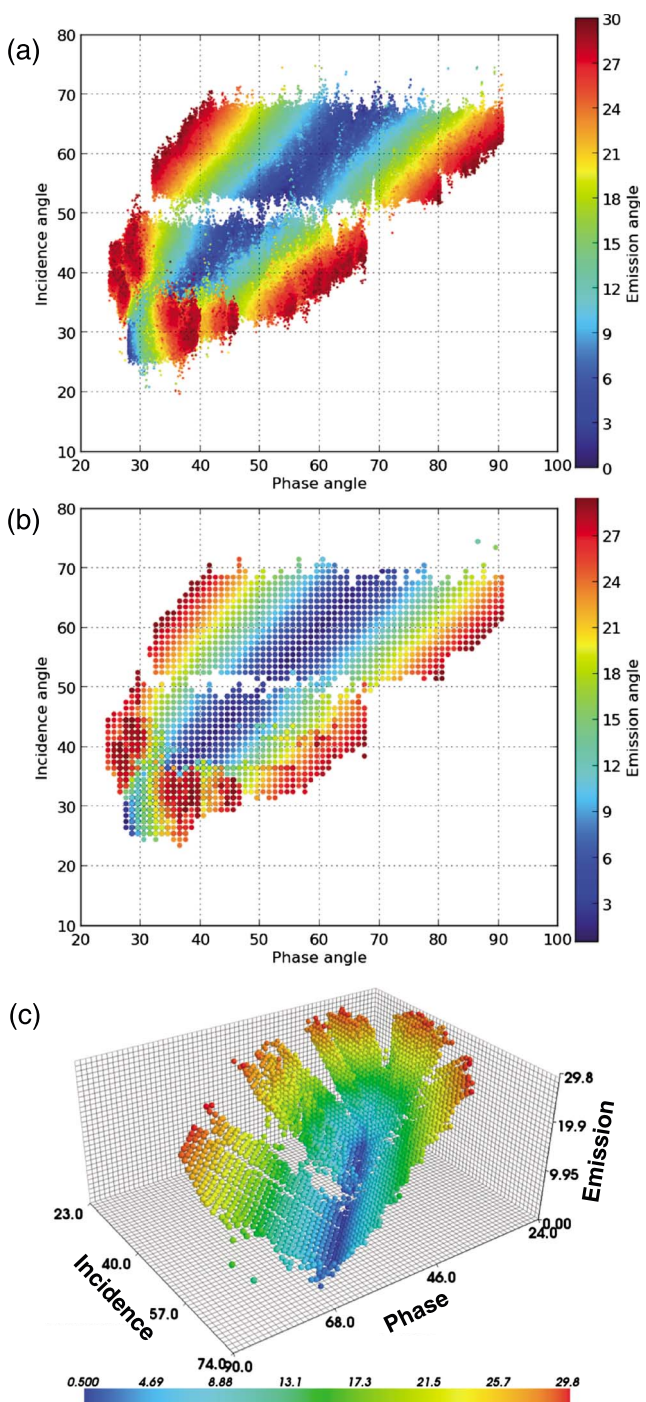


Figure 5. The i , e , and g angle distributions in a sample tile centered at 30.5°N , 297.5°E . (a) The actual WAC observation data, (b) the angle bins generated by angle binning, (c) the 3-D view of the angle bins. The color in Figure 5c corresponds to the emission angle e .

imize the starting value dependence, we used 30 randomly generated starting value, we calculated the optimized parameter set and the Chi-square of fitting residuals for the error return value. The fitting residuals (RW_j) are given by

$$RW_j = \left[\frac{I/F_j}{M_{(P_j, e_j, g_j)}} - 1 \right] N_j \quad (1)$$

beta angle per tile ranges from 0.0° to 15.5° (4.4° in average) and maximum beta angle from 58.0° to 84.9° (Figure 6a, 78.3° in average) for 0° to 360°E , 70°S to 70°N area. The spatial variation of maximum beta angle results in the regional offsets in maximum i and g (Figure 6b). Since the upper limits of i and g affect the model fitting, particularly b and c (see section 2.3), we excluded observations at $g > 97^{\circ}$ and also $i > 75^{\circ}$ to keep the maximum angles high but consistent for most tiles.

Photometric properties differ at the scale of WAC pixels, thus a pixel-by-pixel photometric solution would provide the most accurate normalization. However, the scale for solving the Hapke equation is currently limited to 1° by 1° by the number of repeated observations at varying photometric angles. The LRO orbit ground track separation is greatest at the equator resulting in the fewest number of observations per unit area (relative to higher latitudes). For example, the range in g for the Taurus Littrow valley (Apollo 17 landing site; 19° to 23°N latitude, 28° to 31°E longitude, Figure 7) is from 15.1° to 25.6° (minimum) and 77.0° to 106.2° (maximum) per pixel at $1/64^{\circ}$ pixel scale ($\sim 448\text{ m/pixel}$). These uneven ranges of g at each pixel in this scale result in spatially uneven accuracies in the model fitting. Therefore, we set the tile size to 1° by 1° to maximize the range of g within a tile and to minimize the local variation of g ranges from tile to tile.

In the model fitting for the photometric parameter calculation, we used the Levenberg-Marquardt least-squares minimization algorithm [Gill and Murray, 1978]. Theoretically, this algorithm cannot find a unique global minimum, thus the starting value affects the calculation result. To min-

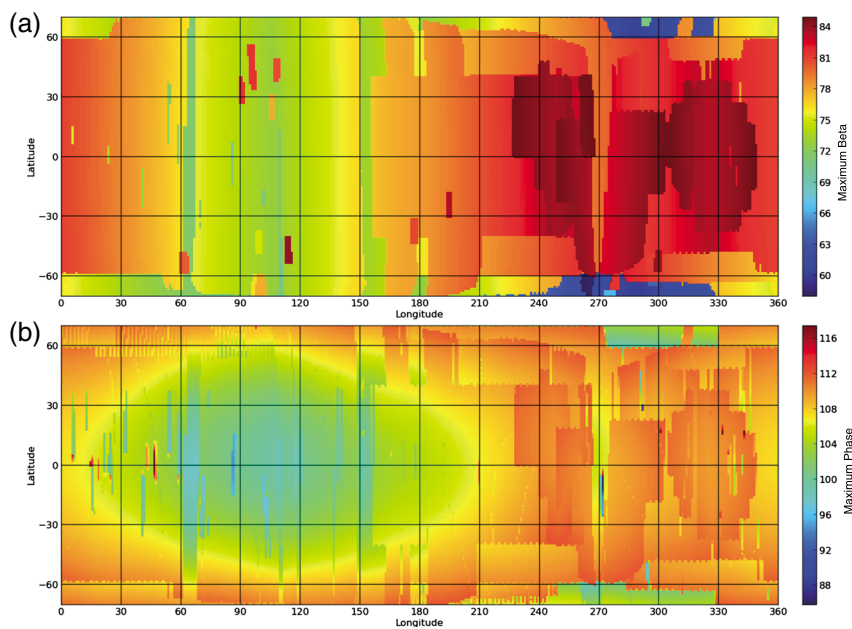


Figure 6. (a) Maximum beta angle in absolute value and (b) maximum phase angle in 643 nm band for 70°S to 70°N, 0° to 360°E, from the WAC data set acquired from February 2010 to October 2011.

where j denotes each bin (derived by the angle binning), I/F_j is the median I/F of each bin, $M_{(P,i_j,e_j,g_j)}$ is the model value with the angles of i , e , and g at the bin center, and P is the model parameter. N_j is the number of data points in each bin and is used to weight the bins. Bins with a relatively high number of observations result in more precise estimates of I/F for each angle condition because the area within the tile is more evenly sampled, and thus small high- or low-reflectance spots have less influence on the bin average. Based on this assumption, the weights result in optimized parameters for the bins with more data points. From the 30 fitting runs with different starting values, we selected the best fitting parameters that provided the minimum fitting residual. Since about 50% of the 30 trial calculations resulted in identical parameters with the minimum fitting residuals, there is a high probability that the fitting algorithm obtained the global minimum.

All of the derived photometric parameters (w , b , c , B_{50} , and h_5 ; see section 2.3) at each tile are stored in a geographic grid matrix (hereafter called “parameter map”). Since the parameters are computed for each wavelength independently, seven individual parameter maps are created for each parameter. The parameter

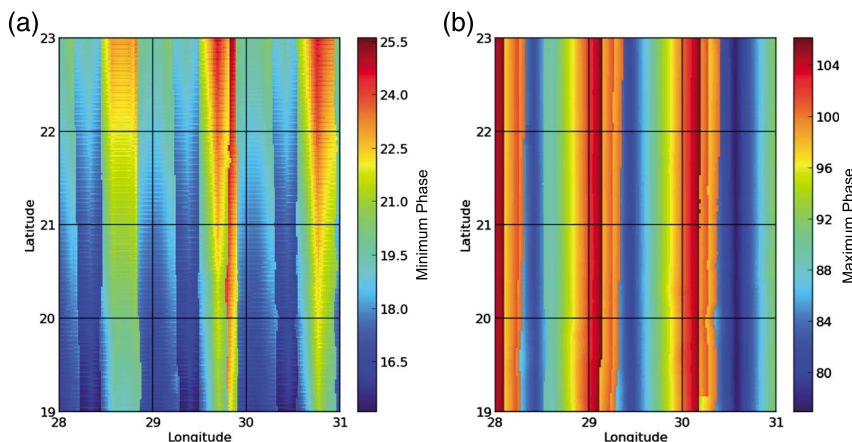


Figure 7. The spatial variations of (a) minimum and (b) maximum phase angles of the WAC data sets (21 months) in 643 nm band at Taurus Littrow. The resolution is 1/64° per pixel.

Table 1. Free Parameters of the Hapke Model^a

Symbols	Name	Value
w	Single scattering albedo	Fitting
b	Henyey-Greenstein double-lobed single particle phase function parameter	Fitting
c	Henyey-Greenstein double-lobed single particle phase function parameter	Equation (2)
B_{C0}	Amplitude of Coherent Backscatter Opposition Effect (CBOE)	0.0
h_C	Angular width of CBOE	1.0
B_{S0}	Amplitude of Shadow Hiding Opposition Effect (SHOE)	Equation (4)
h_S	Angular width of SHOE	Fitting
$\bar{\theta}_p$	Effective value of the photometric roughness	23.4
ϕ	Filling factor	1.0

^a"Fitting" and "Equation (x)" denotes the value calculated by model fitting and by indicated equation respectively.

maps not only enable photometric correction of WAC images but also provide the means to investigate regional variations of photometric properties of the Moon in a geologic context.

2.3. Photometric Model: Simplification and Stepwise Parameter Determination

For the photometric model, we employed the Hapke model (the bidirectional reflectance function proposed by Hapke [1981, 2002, 2008, 2012a]) for several reasons. Compared to empirical photometric models, the Hapke model includes parameters with physical meanings that relate to properties of the surface materials. There are several other photometric models based on physical theory, such as Borel *et al.* [1991], Stamnes *et al.* [1988], Douté and Schmitt [1998], Shkuratov *et al.* [1999], and Mishchenko *et al.* [2002]. Among them, Hapke model is widely used in planetary remote sensing and thus relatively large numbers of preexisting works [Mustard and Pieters, 1989; Clark, 1995; McGuire and Hapke, 1995; Cord *et al.*, 2003; Johnson *et al.*, 2006; Souchon *et al.*, 2011; Johnson *et al.*, 2013; Souchon *et al.*, 2013] already studied the Hapke parameters, which helps to interpret the derived parameters in this study. Also, since each component of this model has a physically defined contribution and is easy to implement or exclude separately, it is helpful to reduce the number of free parameters and apply a step-by-step parameter determination as explained below.

The Hapke model has nine free parameters (w , b , c , B_{C0} , h_C , B_{S0} , h_S , $\bar{\theta}_p$, and ϕ ; see Table 1) in the latest form (see Appendix A). The accurate determination of these nine free parameters directly from the data inversion (model fitting) is difficult due to the mathematical coupling of some parameters [Helfenstein, 1986; Mustard and Pieters, 1989]. Particularly in our tile-by-tile method, the limited range of i and g at high latitudes and the discrete distribution of i , e , and g angles in the fitting data for each tile results in additional uncertainty to the parameter calculation. To minimize these issues, we simplified the original Hapke model based on several assumptions and determined the parameters in a stepwise manner described below.

Theoretically the Coherent Backscatter Opposition Effect (CBOE, described by B_{C0} , h_C) dominates only at very low phase angles ($< 3^\circ$), while the significance of the Shadow Hiding Opposition Effect (SHOE) diminishes approaching 40° phase angle. However, it is difficult to discriminate between CBOE and SHOE only by model fitting [Hapke *et al.*, 2012]; thus, we set CBOE to 1.0 ($B_{C0} = 0$) to avoid competing CBOE and SHOE. This procedure ignores, but does not completely eliminate, the effects of the CBOE. Hence, the SHOE parameters will inevitably be a mixture of the two types of backscatter.

The porosity factor K (described by filling factor ϕ) was set to 1.0 ($\phi = 0$) to avoid mathematical coupling of the single scattering albedo (w) and K , which both control the multiple scattering (equation (A5)) and amplitude of I/F at all photometric angles (equation (A1)). No reference value of ϕ based on laboratory measurement is available [Hapke, 2012a]. Also, to separate w and K from the model fitting is not practical under the limit of $i < 75^\circ$ and $e < 30^\circ$ in the current WAC data set. Accurate determination of ϕ could be possible with future observations acquired at high emission angles of high-reflectance materials.

The Henyey-Greenstein double-lobed single particle phase function (equation (A3)) parameter c was derived as a function of b , written as

$$c = 3.29 \exp(-17.4b^2) - 0.908 \quad (2)$$

This function was obtained from an empirical relation between b and c (called the "hockey stick relation") based on various measurement reports described by Hapke [2012b]. The accurate determination of the

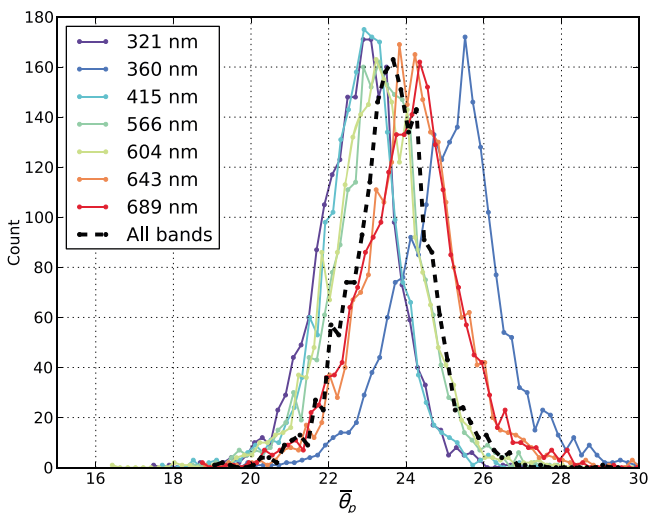


Figure 8. The histograms of $\bar{\theta}_p$ calculated for the tiles inside 3°S to 3°N , 0° to 360°E area. The median of $\bar{\theta}_p$ for all seven wavelength is 23.4° .

free parameters (w , b , B_{50} , h_s , and $\bar{\theta}_p$) were calculated for seven wavelengths at each equatorial tile (2160 total). The derived $\bar{\theta}_p$ from these tiles fell into a near-Gaussian distribution (Figure 8), and the histogram peak (mode) of each band fell within 22.9° to 25.5° . No strong correlation between $\bar{\theta}_p$ and other free parameters or the geologic context was recognized. Theoretically $\bar{\theta}_p$ is independent of wavelength, thus we took a median across the wavelength at each tile then derived the most common value from all the tiles (23.4°) as the final representative constant of $\bar{\theta}_p$.

The B_{50} (amplitude of SHOE) was then interpolated using w , b , and c within the equatorial area (3°S to 3°N latitude), to minimize the influence of the decreasing range of g at high latitudes. The B_{50} is approximated [Hapke, 2012a] by

$$B_{50} \approx \frac{S(0)}{wp(0)} \quad (3)$$

where $S(0)$ is the light scattered into zero phase from the illuminated part of the particle surface, $wp(0)$ is the total light scattered from the particle into zero phase. The $p(0)$ is given by equation (A3) with $g = 0$. The remaining four free parameters (w , b , B_{50} , and h_s) were calculated first for the equatorial tiles, then using w , b , and c , we derived a regression line between w and $S(0)$ which indicates a linear correlation with R^2 value (coefficient of determination) of 0.91 in 643 nm band (Figure 9). The gradient, y -intercept, and R^2 of the linear regression line for each wavelength are shown in Table 2. Using these w versus $S(0)$ correlations, B_{50} was calculated by

$$B_{50} = \frac{\alpha w + \beta}{wp(0)} \quad (4)$$

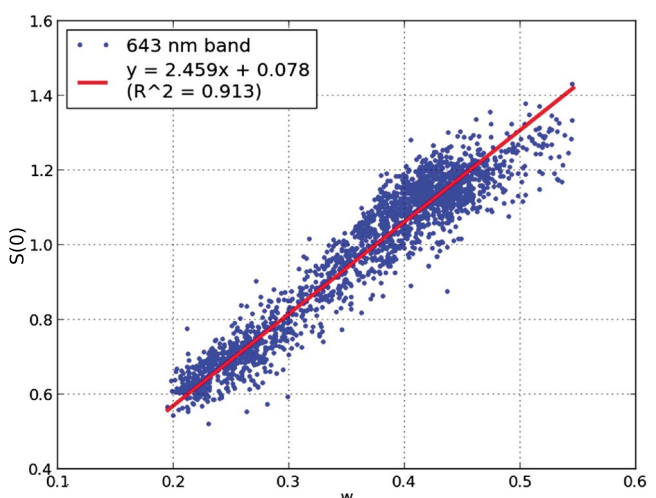


Figure 9. Plots of $S(0)$ versus w in 643 nm band for 3°S to 3°N , 0° to 360°E , and the linear regression line. The gradient, y -intercept, and R^2 value of the regression line for each wavelength is listed in Table 2.

parameter c requires wide range of g , especially greater than 90° (up to 180°) to detect forward scattering. The maximum g in the WAC observation goes up to about 120° , but due to the spatial variation of the maximum g as mentioned above, we limited g up to 97° to keep the maximum g constant across most of the tiles. Since the range of $g < 97^{\circ}$ is not sufficient to precisely determine c by model fitting, c estimation by equation (2) was utilized.

The roughness parameter $\bar{\theta}_p$ was set to a constant value to avoid mathematical coupling between w and $\bar{\theta}_p$. The constant value of $\bar{\theta}_p$ was derived from an equatorial area (3°S to 3°N , 0° to 360°E), where the maximum range of i and g are available. The five

Table 2. The Gradient, Y-Intercept, and R^2 Values of the Linear Regression Line of $S(0)$ as a Function of w for Each Wavelength

Wavelength [nm]	Gradient (α)	Y-Intercept (β)	R^2
321	3.378	0.064	0.896
360	3.423	0.030	0.902
415	2.646	0.124	0.874
566	2.332	0.131	0.891
604	2.438	0.096	0.910
643	2.459	0.078	0.913
689	2.310	0.103	0.908

observation with parameter set P , and $M_{(P,i_s,e_s,g_s)}$ is the modeled radiance factor at the standard angles of i_s , e_s , and g_s . The parameter set P of the Hapke model is looked up from the parameter map at the corresponding tile. For the standard angles, we used $i = g = 60^\circ$, $e = 0^\circ$ instead of the traditional angles of $i = g = 30^\circ$, $e = 0^\circ$ that is used for most of the planetary remote sensing data [e.g., McEwen and Robinson, 1997; Haruyama et al., 2008; Otake et al., 2010; Yokota et al., 2011; Besse et al., 2013; Wu et al., 2013] and laboratory measurements [Pieters and Englert, 1993; Cloutis et al., 2006]. Since at high latitudes the range of i and g are limited to relatively high values (latitude is a rough proxy for the lower limit of i and g), we normalized to 60° to avoid extrapolation within the high-latitude tiles.

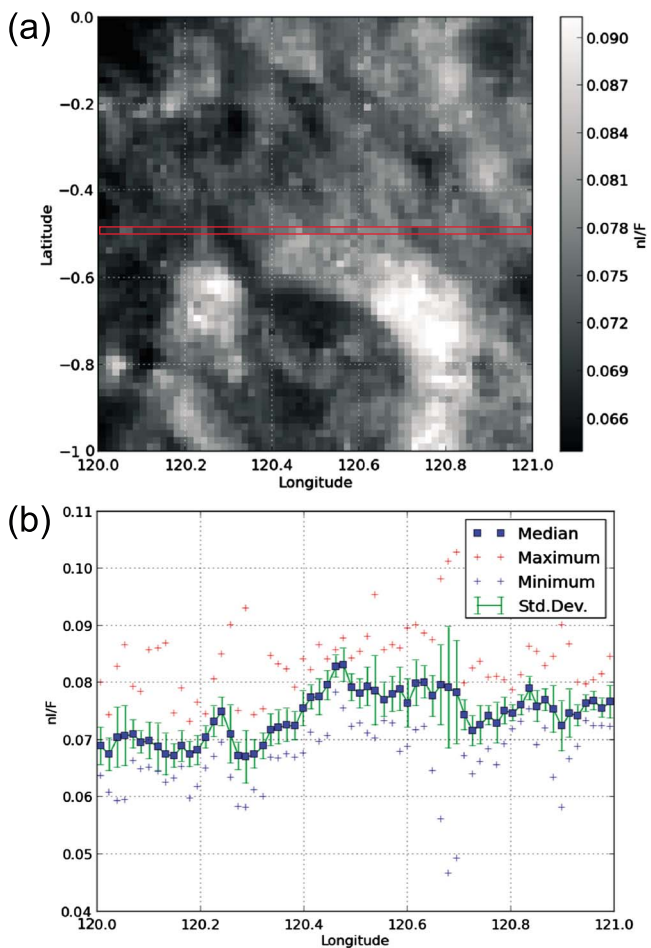


Figure 10. Schematic diagram of the median and the standard deviation calculations for each $1/64^\circ$ scale subsection within the tile centered at 0.5°S , 120.5°E . (a) The median map of nl/F in 643 nm, and (b) cross section along a line framed by red box in Figure 10a.

In summary, we reduced the original nine free parameters (w , b , c , B_{C0} , h_C , B_{S0} , h_S , $\bar{\theta}_p$, and ϕ) to three free parameters (w , b , and h_S). These remaining free parameters were calculated by the model fitting for each tile at 70°S to 70°N latitude, 0° to 360°E longitude area.

2.4. Photometric Normalization and Error Analysis

The photometrically normalized radiance factor (nl/F) is given by

$$nl/F = \frac{I/F}{M_{(P,i,e,g)}} \quad (5)$$

where I/F is observed radiance factor, $M_{(P,i,e,g)}$ is the modeled radiance factor at the same i , e , and g as the

is the modeled radiance factor at the standard angles of i_s , e_s , and g_s . The parameter set P of the Hapke model is looked up from the parameter map at the corresponding tile. For the standard angles, we used $i = g = 60^\circ$, $e = 0^\circ$ instead of the traditional angles of $i = g = 30^\circ$, $e = 0^\circ$ that is used for most of the planetary remote sensing data [e.g., McEwen and Robinson, 1997; Haruyama et al., 2008; Otake et al., 2010; Yokota et al., 2011; Besse et al., 2013; Wu et al., 2013] and laboratory measurements [Pieters and Englert, 1993; Cloutis et al., 2006]. Since at high latitudes the range of i and g are limited to relatively high values (latitude is a rough proxy for the lower limit of i and g), we normalized to 60° to avoid extrapolation within the high-latitude tiles.

Using the nl/F derived from 21 months of WAC observations, we produced a multispectral and multitemporal mosaic for 0° to 360°E longitude, 70°S to 70°N latitude with 64 pixel/degree resolution (473.8 m/pixel at the equator). Each pixel of this mosaic is the median of nl/F derived from multiple observations, that satisfy $g < 97^\circ$, $i < 75^\circ$. For the mosaic pixels with no observations in this angle range (such as pole-facing crater walls at the high latitudes), we used nl/F from $g \geq 97^\circ$, $i \geq 75^\circ$ observations to avoid pixels with no suitable observations. A schematic diagram of the production of this mosaic (hereafter called “median mosaic”) is shown in Figure 10.

The model fitting accuracies were evaluated by calculating the coefficient of determination (R^2) and the standard deviation of the fitting residuals (σ_m). R^2 was computed using the I/F that went through the albedo filtering (see section 2.2) for each tile. Fitting residuals (RE) were computed by

$$RE = \frac{I/F}{M_{(P,i,e,g)}} - 1 \quad (6)$$

Then the standard deviation of RE was computed for each $1/64^\circ$ scale

subsection (hereafter denoted as $\sigma_{1/64}$, see Figure 10, green error bars) within a tile (4096 subsections total, same resolution as the median mosaic) in order to minimize the scatter due to albedo variation within a tile. σ_m was given by the median of $\sigma_{1/64}$ for all subsections at each tile. The maps of the standard deviation of RE for each $1/256^\circ$ scale subsection ($\sigma_{1/256}$, 65,536 subsections total within a tile) were also computed for the sample tiles (one tile from the mare and another from the highland) using full resolution 643 nm band images, to assess the dominant factor increasing the fitting residuals.

We used $i = g = 60^\circ$, $e = 0^\circ$ as the standard angles for normalization instead of traditional angles ($i = g = 30^\circ$, $e = 0^\circ$) as mentioned above. Due to the difference of photometric properties at each geologic unit, the nI/F using 30° of i, g and the nI/F using 60° or other standard angles of i, g can cause spatial offsets in nI/F depending on the geologic units. We examined such nI/F differences caused by the standard angles by calculating $D_{(s1,s2)}$.

$$D_{(s1,s2)} = \frac{nI/F_{s1}}{nI/F_{s2}} = \frac{\frac{I/F}{M_{(P,i,e,g)}} M_{(P,i_{s1},e_{s1},g_{s1})}}{\frac{I/F}{M_{(P,i,e,g)}} M_{(P,i_{s2},e_{s2},g_{s2})}} = \frac{M_{(P,i_{s1},e_{s1},g_{s1})}}{M_{(P,i_{s2},e_{s2},g_{s2})}} \quad (7)$$

$D_{(s1,s2)}$ is the ratio of nI/F computed over the range of g_{s1} from 0° to 70° ($= s1$) to nI/F calculated with $g_{s2} = 30^\circ$ ($= s2$). In both cases $e_s = 0^\circ$ and $i_s = g_s$. The $D_{(s1,s2)}$ was calculated for all seven wavelengths. For the photometric parameter P , we used multiple parameter sets from 3600 tiles within the equatorial area ($\pm 5^\circ N$). Note that the equatorial area receives the widest range of i, g , thus has better fitting curves throughout 0° to 70° in i, g ranges relative to high latitudes.

2.5. Offsets Along Tile Boundaries

Since the tile-by-tile method utilizes varying values for the Hapke model parameters at each tile, the pixels normalized by two discrete parameter sets are located next to each other along tile boundaries. This discrete step of the photometric parameters can introduce a systematic offset of nI/F . Noticeable offsets might occur at a geologic unit which has homogeneous photometric properties, located across the tile boundaries.

We investigated the actual magnitude of such offsets by characterizing the amplitude of the nI/F offset (A), that is derived by

$$|nI/F_1 - nI/F_2| = \left| \frac{I/F}{M_{(P_1,i,e,g)}} M_{(P_1,i_s,e_s,g_s)} - \frac{I/F}{M_{(P_2,i,e,g)}} M_{(P_2,i_s,e_s,g_s)} \right| \quad (8)$$

$$I/F * A = I/F \left| \frac{M_{(P_1,i_s,e_s,g_s)}}{M_{(P_1,i,e,g)}} - \frac{M_{(P_2,i_s,e_s,g_s)}}{M_{(P_2,i,e,g)}} \right| \quad (9)$$

Thus A is given by

$$A = \left| \frac{M_{(P_1,i_s,e_s,g_s)}}{M_{(P_1,i,e,g)}} - \frac{M_{(P_2,i_s,e_s,g_s)}}{M_{(P_2,i,e,g)}} \right| \quad (10)$$

where P_1 and P_2 denote the parameter sets from two adjacent tiles, nI/F_1 and nI/F_2 are the nI/F derived by P_1 and P_2 , respectively. The actual offset between the two nI/F is given by $I/F * A$ (equation (9)). For every single tile boundary the A was calculated using about 8000 to 10,000 sets of i, e, g from the WAC observations adjacent (distance less than $1/64^\circ$; ~ 473.8 m at equator) to the boundary line. Then the median (A_m), standard deviation (A_s), and maximum values (A_{\max}) of A were derived for these angle sets. Each tile shares four boundaries with four neighboring tiles, and tile size is currently 1° by 1° for 0° to $360^\circ E$ longitude and $70^\circ S$ to $70^\circ N$ latitude areas, thus 50,260 ($= 359 \times 140$) vertical, 50,040 ($= 139 \times 360$) horizontal tile boundaries were calculated in total.

3. Results

3.1. Normalized Mosaic

Within the photometrically normalized near-global WAC mosaic (the median mosaic, see section 2.4; Figure 11a), no obvious color artifacts are visible along the tile boundaries (see Figures 12a–12c), indicating that tile boundary reflectance offsets (dominantly $\leq 1\%$, see section 3.3 for tile boundary offset details) are smaller than the geologic reflectance variations. Also, no color artifacts are recognizable from pole to pole

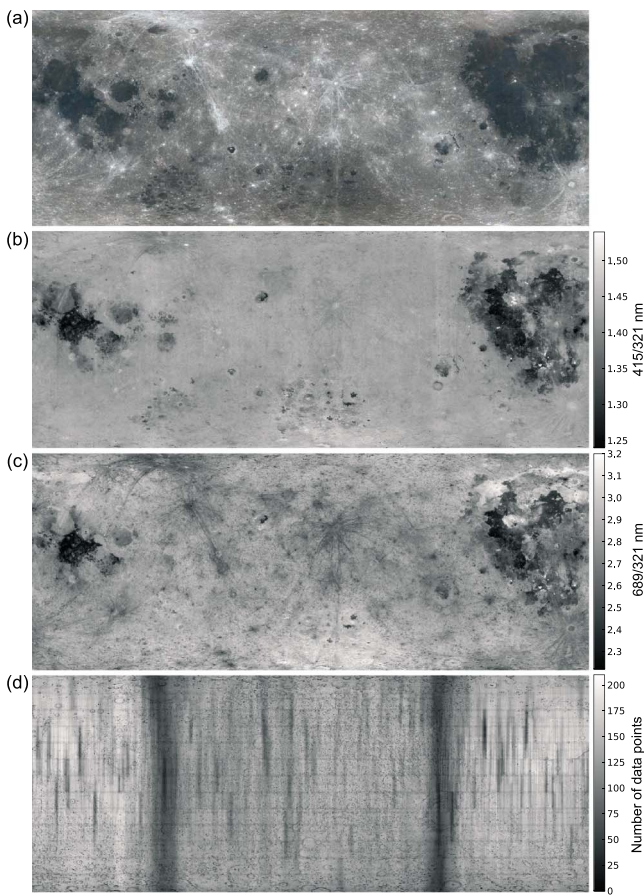


Figure 11. (a) The median mosaic (median of nI/F from 21 months WAC data) in RGB color composite (red:689 nm, green:415 nm, blue:321 nm), (b) ratio map of 415/321 nm bands, (c) ratio map of 689/321 nm bands, and (d) number of data points used for each 1/64°-sized pixel (473.8 m/pixel at the equator) in 689 nm band, for 70°S to 70°N, 0° to 360°E in equirectangular map projection.

high ilmenite contents [Lucey et al., 1998; Robinson et al., 2010, 2011]. Variations in 689/321 nm band ratio (Figure 11c) represent spectral slopes dominantly controlled by the relative abundances of iron and titanium (mostly within pyroxene, olivine, and ilmenite) and the state of maturity [Lucey et al., 2000]. Along two longitude bands, $83^{\circ} \pm 10^{\circ}$ E and $266^{\circ} \pm 7^{\circ}$ E, relatively noisy and higher ratio values occur (4–27% above the surroundings) expressed as faint vertical stripes (about 1° to 1.5° in width, Figure 12d). Also, in these areas, several square-shaped artifacts are apparent, which are due to poor fitting in that tile (upper half of Figure 12d). These longitude bands have a paucity of image data as the spacecraft was yawed 90° for monthly station keeping maneuvers (delta-v burns) during which no image data was obtained (Figure 11d; hereafter called delta-v zone, see Appendix B). Additionally, all the observations in this band were obtained in solely ascending orbits for $83^{\circ} \pm 10^{\circ}$ E band and in descending orbits for $266^{\circ} \pm 7^{\circ}$ E band, thus emphasizing any remaining residuals in the temperature sensitivity correction [Sato et al., 2013].

3.2. Model Fitting Accuracy

The tile map of R^2 (determination coefficient of RE) for 70°S to 70°N latitude, 0° to 360°E longitude area (Figure 13a) illustrates the overall high goodness of fit to the actual data points. The median and standard deviation of R^2 for all the tiles are 0.96 and 0.063 respectively for the 643 nm band. In the histogram (Figure 13c), 81.3% of the tiles have $R^2 > 0.9$. The highland/mare boundaries, for example, the western edge of Oceanus Procellarum, surrounding edges of Mare Serenitatis, Crisium, and Orientale, show relatively lower R^2 (0.9 to 0.95) than those tiles contained entirely within the maria (0.98 to 0.99) and the surrounding highlands at comparable latitudes. These lower R^2 at geologic unit boundaries are due to the distinctly

(Figure 11a), indicating that the decrease in the range of i and g angles toward high latitudes does not significantly affect the nI/F derived by the tile-by-tile method. Since the i, e, g angles were calculated from the 100 m scale WAC GLD100 [Scholten et al., 2012], the mosaic theoretically represents surface reflectance independent of topographic relief. Inside some craters at high latitudes (poleward of 60°S and 60°N), systematic artifacts are found, particularly along the pole facing slopes. These artifacts are due to the large fraction of i with values more than 90° (shadows) that result in invalid nI/F values. These locations will need exception handling to avoid anomalous values to improve the quality of mosaic product.

The ratio maps of 415/321 nm and 689/321 nm (Figures 11b and 11c) are useful indicators of compositional and maturity differences. The 415/321 nm ratio represents spectral slope that decreases dominantly with the ilmenite content of the surface [Wagner et al., 1987; Cloutis et al., 2008; Robinson et al., 2010]. The central and eastern areas of Oceanus Procellarum, western portion of Mare Imbrium, and Mare Tranquillitatis have low ratio values (between 1.25 and 1.30), consistent with relatively

high ilmenite contents [Lucey et al., 1998; Robinson et al., 2010, 2011]. Variations in 689/321 nm band ratio (Figure 11c) represent spectral slopes dominantly controlled by the relative abundances of iron and titanium (mostly within pyroxene, olivine, and ilmenite) and the state of maturity [Lucey et al., 2000]. Along two longitude bands, $83^{\circ} \pm 10^{\circ}$ E and $266^{\circ} \pm 7^{\circ}$ E, relatively noisy and higher ratio values occur (4–27% above the surroundings) expressed as faint vertical stripes (about 1° to 1.5° in width, Figure 12d). Also, in these areas, several square-shaped artifacts are apparent, which are due to poor fitting in that tile (upper half of Figure 12d). These longitude bands have a paucity of image data as the spacecraft was yawed 90° for monthly station keeping maneuvers (delta-v burns) during which no image data was obtained (Figure 11d; hereafter called delta-v zone, see Appendix B). Additionally, all the observations in this band were obtained in solely ascending orbits for $83^{\circ} \pm 10^{\circ}$ E band and in descending orbits for $266^{\circ} \pm 7^{\circ}$ E band, thus emphasizing any remaining residuals in the temperature sensitivity correction [Sato et al., 2013].

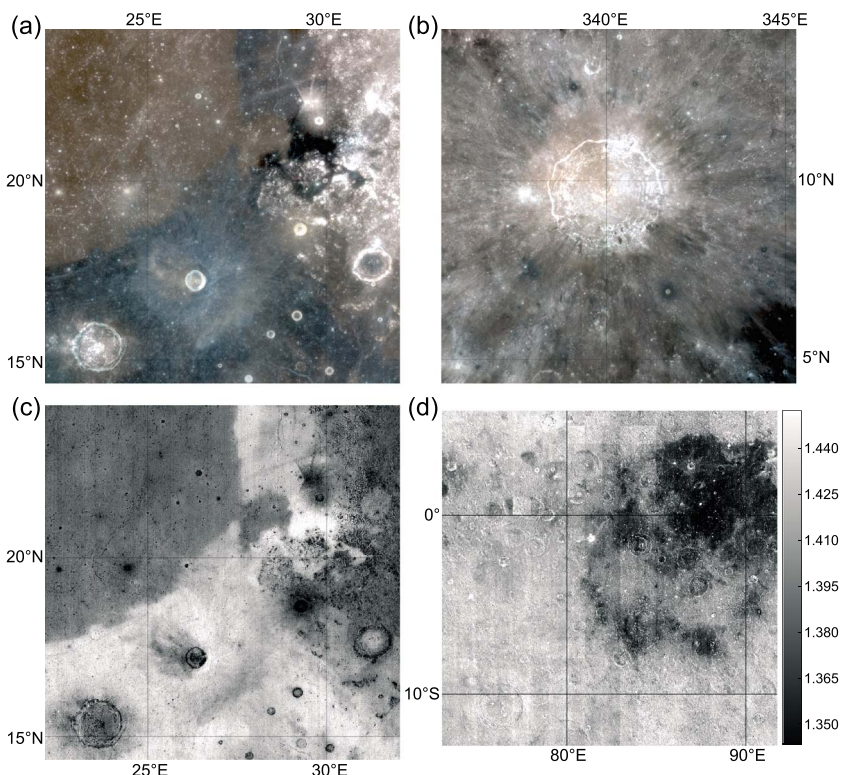


Figure 12. The median mosaic in $1/64^\circ$ per pixel resolution (red:689 nm, green:415 nm, blue:321 nm) near (a) Apollo 17 landing site and (b) Copernicus crater. The ratio map of (c) 321/415 nm bands near Apollo 17 landing site exhibiting Ti abundance, and (d) 415/321 nm bands near Mare Smythii representing the faint vertical stripes and the blocky noise.

bimodal albedo populations inside each tile along the highland/mare boundaries. The albedo filtering selects one dominant albedo mode to fit, which improves fitting accuracy. Compared to the monomodal albedo tiles, however, fewer data points over a smaller range of angles are used for the bimodal albedo tiles, thus resulting in relatively lower R^2 values. The median and standard deviation of R^2 in the other six wavelengths ranges from 0.959 to 0.967 and from 0.059 to 0.073 respectively, and shows similar histogram curves and spatial variations as the 643 nm band.

The σ_m (Figure 13b) indicates the consistency of nl/F derived from observations with varying i , e , and g angles at the same spot (within each $1/64^\circ$ scale subsection) of the surface. If the region within a tile was perfectly homogeneous in its photometric properties, identical nl/F values would be derived for each $1/64^\circ$ subsection within that tile by one parameter set, thus the σ_m would be zero. For tiles with photometric heterogeneities (induced by variations in composition, maturity, grain size, etc.), the parameter set does not provide the same level of accuracy for all subsections within that tile. The median and standard deviation of σ_m for all the tiles are 0.041 ± 0.0037 and 0.0092 ± 0.0011 respectively, for all the wavelengths. The mare-dominated tiles in this figure have distinctly lower σ_m (about 0.027) than the highland tiles (0.044 in average), resulting in the bimodal histogram of σ_m (Figure 13d). The maps of $\sigma_{1/256}$ (σ for each $1/256^\circ$ per pixel block, 118.5 m/pix resolution, Figure 14) near the northern edge of Mare Fecunditatis exhibit higher $\sigma_{1/256}$ within the highland tile (Figure 14b) relative to the mare tile (Figure 14a). The average $\sigma_{1/256}$ is 0.049 for the mare tile and 0.058 for the highland tile which translate into percent uncertainty of 4.9% and 5.8%, respectively. Locally higher reflectance spots, such as immature ejecta deposits, eroded mound crests, and resurfaced slopes do not necessarily coincide with the high $\sigma_{1/256}$ spots (Figures 14e and 14f). The high $\sigma_{1/256}$ spots are predominantly coincident with small-scale morphologies such as craters (< 2 km in diameter), mounds, narrow channels, and sharp contacts between a flat plane and a steep slope. These topographic undulations and facets are not large enough to be resolved in the GLD100 WAC stereo DTM, resulting in smoothing of slopes (Figures 14c and 14d) that increases uncertainty in estimates of i , e , and thus the fitting residuals. Notice that even though GLD100 data set is prepared in 100 m/pix, the effective resolution (minimum horizontal scale of the topographic feature visible in the DTM) is $\sim 300\text{--}500$ m

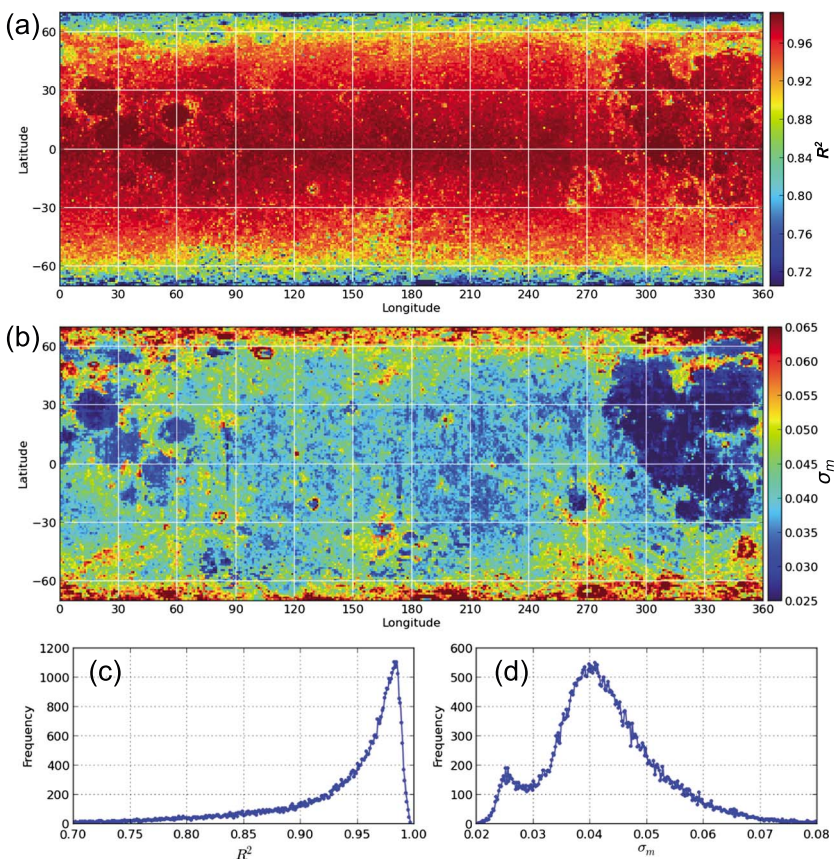


Figure 13. The tile maps of (a) coefficient of determination R^2 , (b) the standard deviation of residuals σ_m , and the histograms of (c) R^2 and (d) σ_m in 643 nm band for 70°S to 70°N, 0° to 360°E.

due to the smoothing effects during the DTM production [Scholten *et al.*, 2012]. Slopes large enough to be resolved by the WAC DTM typically exhibit lower $\sigma_{1/256}$ values (indicated by the arrows in Figures 14b and 14d) where the photometric angles were calculated accurately based on the DTM. Not only the fitting residuals but also the median of n/F (used in the median mosaic, see section 2.4) could be locally altered by small amounts due to the higher uncertainties in the photometric angles. Accuracy of n/F from the small-scale topographic roughness could be improved with higher resolution DTMs (e.g., LROC Narrow Angle Camera DTM ~ 2 m sampling; [Tran *et al.*, 2010], Kaguya Terrain Camera DTM ~ 7.4 m sampling; [Haruyama *et al.*, 2012]).

The R^2 typically decreases from 0.99 to 0.85, and the σ_m increases from 0.038 to 0.055 toward the pole, both indicating increasing uncertainties toward high latitudes particularly beyond 60°N and 60°S. Random scatter in I/F due to subpixel shadows and imperfect calculations of i, e, g (not due to the albedo variation within a tile) could be a significant factor increasing the fitting residuals (thus decrease in R^2 and increase in σ_m) toward the pole. The amplitude of such random scatter is nearly constant for whole i and g ranges whereas the dominant trend of I/F and the fitted model decreases as i increases, approaching zero near $i = 90^\circ$. The division of I/F by the model to derive n/F (see equation (5)) thus amplifies the scatter toward the high i angles. Since high-latitude tiles receive more observations at high i relative to the equator, the amplified scatter dominate the fitting data, contributing to the decrease in R^2 at high latitudes. The decrease in i and g variations at lower values toward the pole also adds uncertainties in the fitting procedure, resulting in relatively increased σ_m .

The model fitting and the normalizing accuracies will be improved as the WAC continues to acquire more observations and the beta angle variation increases within each tile (supplemented with off-nadir observations at higher latitudes to increase the range of phase angle). As the upper limit of g and beta angles (Figure 6) for all tiles are increased to evenly higher values, available ranges of i and g (currently $i < 75^\circ$ and

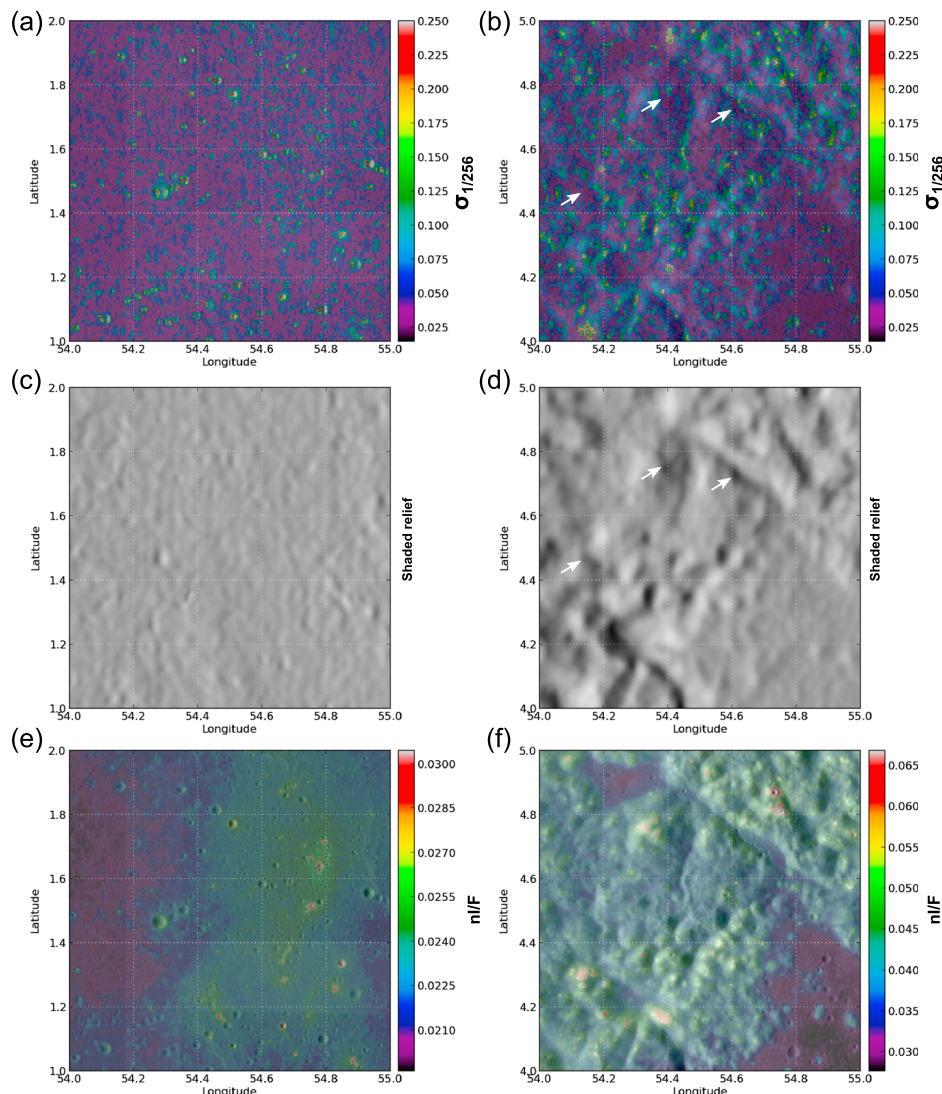


Figure 14. (a and b) Maps of $\sigma_{1/256}$ (~ 118.5 m/pix), (c and d) shaded relief maps (100 m/pix) computed from WAC stereo DTM (GLD100), (e and f) the median of nl/F maps (~ 118.5 m/pix). Figures 14a, 14c, and 14e are for the mare tile centered at 1.5°N , 54.5°E , and Figures 14b, 14d, and 14f are for the highland tile centered at 4.5°N , 54.5°E . Figures 14a and 14b are overlaid on the shaded relief (Figures 14c and 14d). Figures 14e and 14f are overlaid on a WAC monochrome basemap (100 m/pix). The grid size is 0.2° by 0.2° (about 6 by 6 km). Arrows indicate low $\sigma_{1/256}$ spots on the smooth slopes.

$g < 97^\circ$) will increase, improving the fitting accuracy at high latitudes. Higher spatial variations of g enable higher resolutions of the parameter maps, which minimize the surface heterogeneity inside a tile. Additional WAC observations will also improve accuracy of the radiometric calibration, which reduces the artificial scatterers. Further improvements to the stereo DTM [Scholten *et al.*, 2012] will allow more precise angles to be calculated, globally improving the fitting accuracy.

3.3. Offsets Along Tile Boundaries

The A_m (the median of A at each tile boundary, A : amplitude of nl/F offset, see equation (10)) and A_s (the standard deviation of A at each tile boundary) for the 643 nm band (Figures 15a and 15b) are 0.0025 and 0.0034 in average, respectively, for all tile boundaries, which correspond to the offsets of 0.25% and 0.34% relative to each I/F . For the seven wavelength, A_m ranges from 0.0023 to 0.0028 and A_s ranges from 0.0032 to 0.0047. The histogram of A_m (Figure 15c, blue line) indicates that 97.5% of the tile boundaries have an offset of less than 0.01, meaning that the nl/F offsets along the tile boundaries are dominantly $\leq 1\%$. The A_m map (Figure 15a) consists of random noise with no clear regional variation, except beyond 60° latitudes. The A_s map (Figure 15b) is also noisy and shows increasing trend toward the pole and with lower noise within

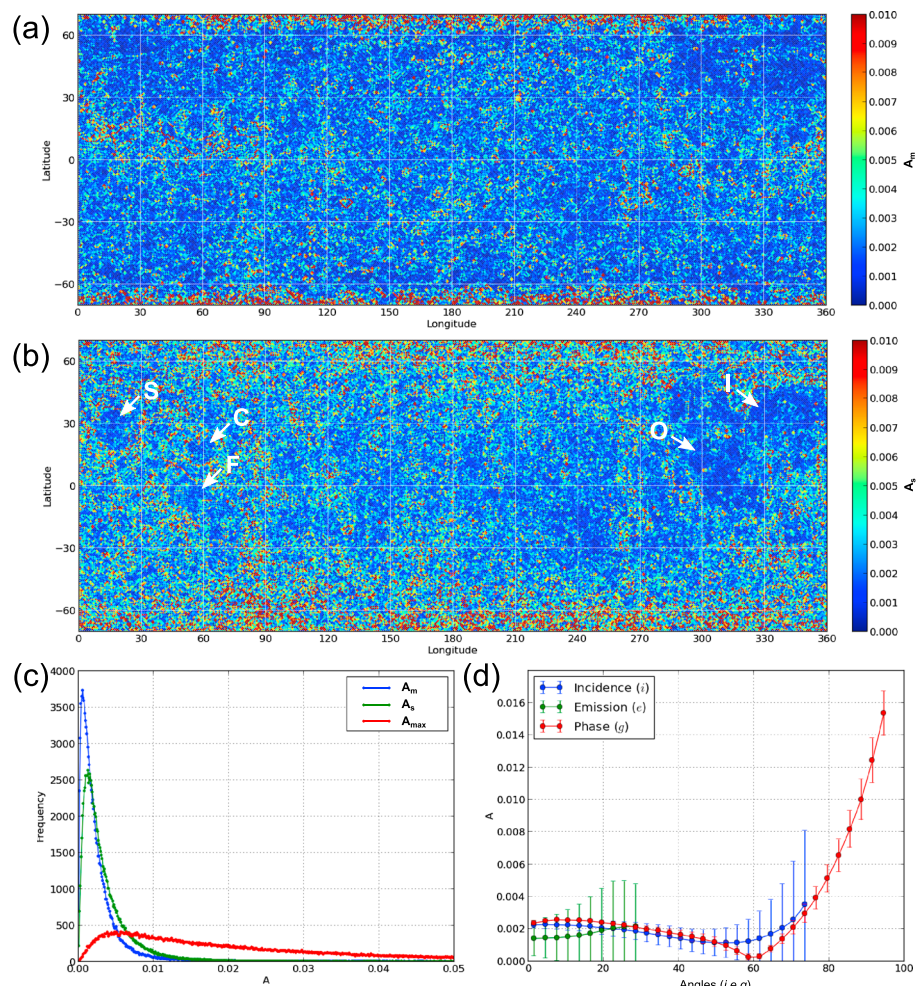


Figure 15. The amplitude of tile boundary offsets A for 70°S to 70°N, 0° to 360°E in 643 nm band. (a) A_m : median of A and (b) A_s : standard deviation of A for each tile boundary, in equirectangular map projection. Arrows with letter indicate the locations of maria with lower noise (Mare Serenitatis: S, Crisium: C, Fecunditatis: F, Oceanus Procellarum: O, and northern Imbrium: I). (c) The histograms of A_m (blue), A_s (green), and A_{\max} : maximum of A for each tile boundary (red), and (d) A at each 3° bin of i , e , and g angles for all the tile boundaries. The dot and error bar in Figure 15d indicate median and standard deviation, respectively.

several maria (e.g., Mare Serenitatis, Crisium, Fecunditatis, Oceanus Procellarum, and northern Imbrium, indicated by white arrows). The histogram of A_{\max} (the maximum of A for each tile boundary, Figure 15c red line), indicates larger frequency for $A_{\max} > 0.01$ compared to the A_m (blue line) or A_s (green line) at > 0.01 . The A at each 3° bin of i , e , and g angles for all tile boundaries are shown in Figure 15d. The minimum A for each i , e , and g angles is found near the standard angles ($i = g = 60^\circ$, $e = 0^\circ$), as expected from its definition (equation (10)). The largest A is found near the upper limit of each angle ($i = 75^\circ$, $e = 30^\circ$, $g = 97^\circ$). In fact, almost all of the A_{\max} values in Figure 15c are obtained at $i = 75^\circ$ and $g = 97^\circ$, which are consistent with Figure 15d. The fitting accuracy near the edge of variable (i , e , and g) ranges decreases relative to the midrange, resulting in the maximum A near the upper limit of the fitting data. The increasing trend of A towards the pole (A_m from 0.0025 to 0.0047 in average; Figure 15a, A_s from 0.0027 to 0.0053 in average; Figure 15b) reflects the same trend of Figure 15d, since the average of i and g increases with latitude. Also, the decreasing variation in i and g toward the pole increases the fitting uncertainties and likely induces a stochastic fluctuation in the parameter maps at high latitudes, which increases A .

3.4. Photometric Parameter Maps

The parameter maps of w , b , c , B_{50} , and h_S for the 643 nm band from 0° to 360°E longitude, 70°S to 70°N latitude area are shown in Figure 16. The w (single scattering albedo) in Figure 16a is correlated to n/F as

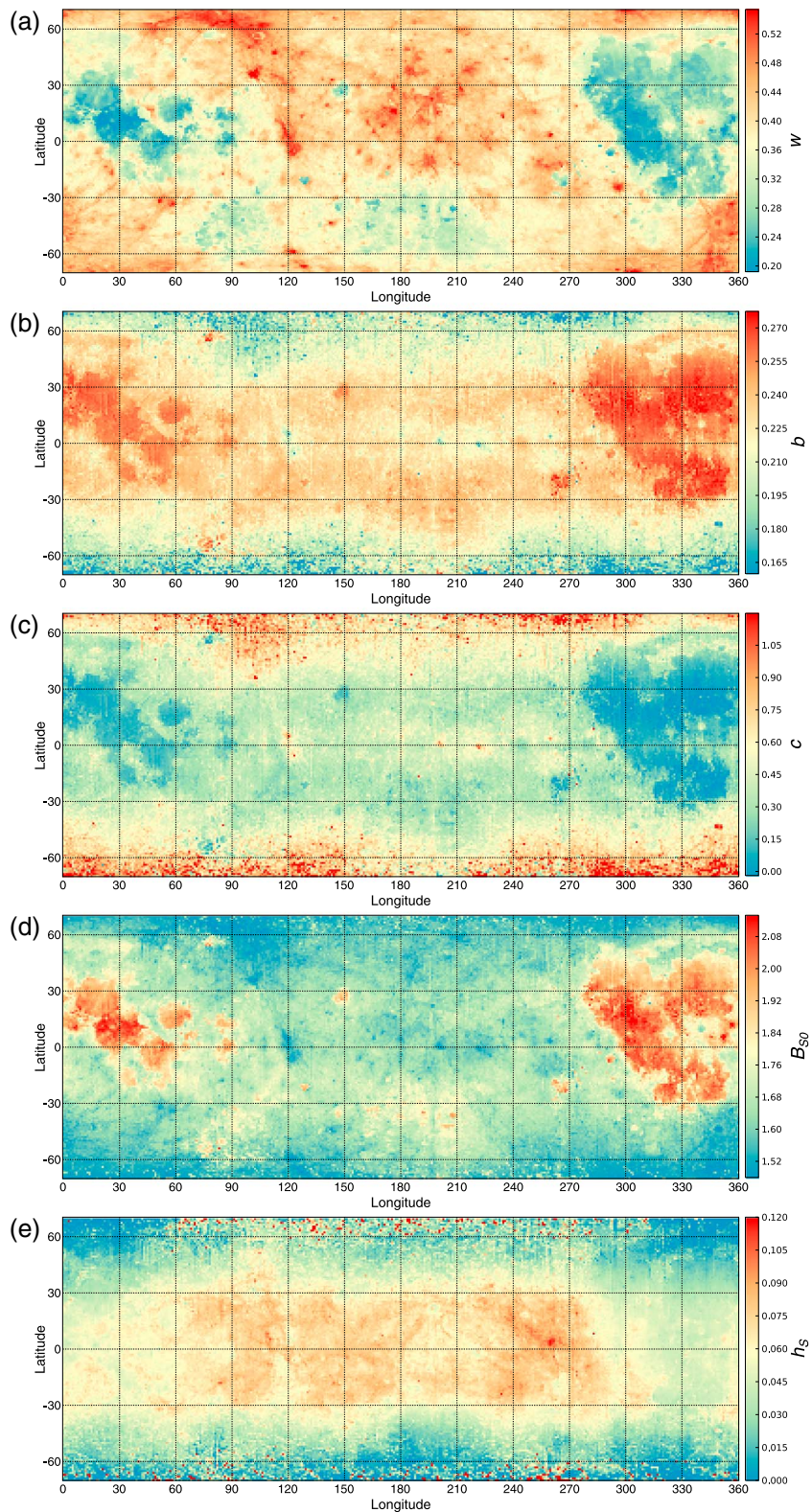


Figure 16. The parameter maps of (a) w , (b) b , (c) c , (d) B_{50} , and (e) h_S in 643 nm band for 70°S to 70°N, 0° to 360°E.

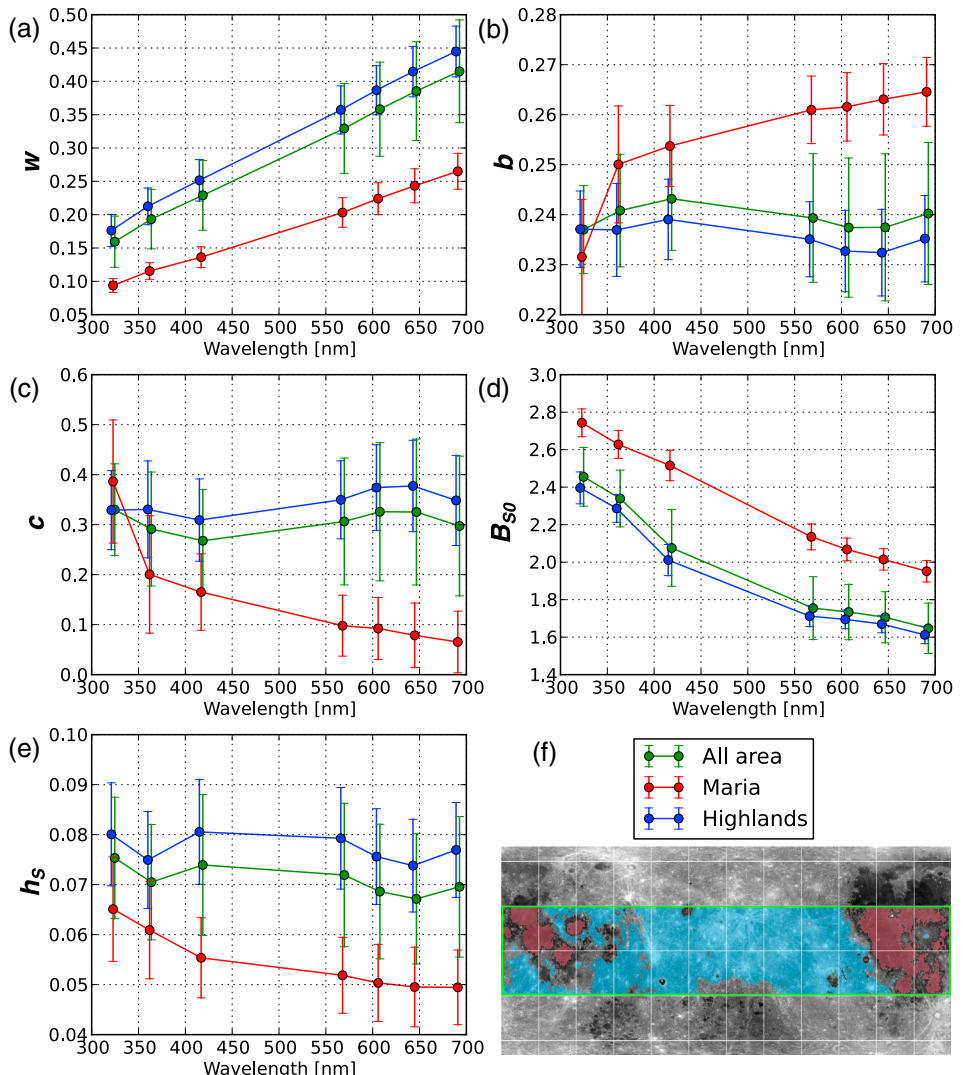


Figure 17. The regional trend of the parameters (a) w , (b) b , (c) c , (d) B_{50} , and (e) h_s as a function of wavelength. (f) Illustration of the colors in Figures 17a–17e which indicate the region of the highlands (blue), the maria (red), and all area (green), inside 30°S to 30°N , 0° to 360°E . The white grid size in Figure 17f is 30° . The dot and error bar in Figures 17a–17e correspond to the median and the standard deviation of the parameters in the parameter map in each region and each wavelength.

expected (see section 4 for a detailed comparison). Note that B_{50} (amplitude of SHOE) given by equation (4) is based on the negative correlation between B_{50} and w at the equator, thus B_{50} (Figure 16d) is essentially an inverse of w (Figure 16a). Also, c (Henyey-Greenstein phase function parameter) is given by equation (2) that is negatively correlated with b , thus Figure 16c shows an inverse trend to Figure 16b.

The parameter b (Figure 16b) is typically high (thus low in c) within the maria (0.26 ± 0.01) relative to the highlands (0.23 ± 0.01). Since c represents the fraction of backward to forward scattering in equation (A3), the lower c in the maria indicates decreased backscattering relative to the highlands. The highland equatorial region ($\pm 15^{\circ}\text{N}$) bounded by longitudes 110°E to 270°E exhibits several low b (0.20 ± 0.02) and high c (0.7 ± 0.3) units (higher backscattering). These anomalies correspond to relatively young craters, such as Necho ($5.21^{\circ}\text{S}, 123.30^{\circ}\text{E}$), King ($4.87^{\circ}\text{N}, 120.45^{\circ}\text{E}$), Vavilov ($0.82^{\circ}\text{S}, 221.22^{\circ}\text{E}$), Stein L ($4.64^{\circ}\text{N}, 180.13^{\circ}\text{E}$), and Korolev X ($0.56^{\circ}\text{N}, 200.58^{\circ}\text{E}$).

The h_s (angular width of SHOE) in Figure 16e typically shows lower values (0.050 ± 0.008) for the maria relative to the highlands (0.074 ± 0.009), except at latitudes poleward of about 40°N and 40°S . The highest h_s spot is located on a young unnamed crater (9.4 km in diameter) and the surrounding areas at 3.30°N ,

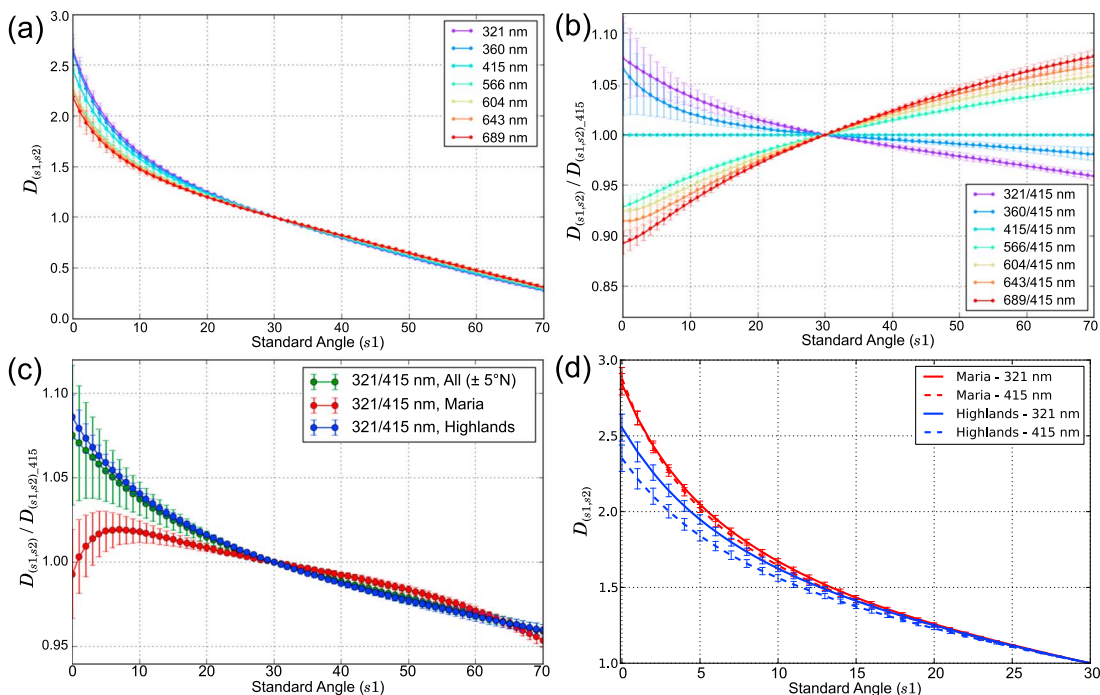


Figure 18. Plots of (a) $D_{(s1,s2)}$ (n/F differences caused by the standard angle change, equation (7)) as a function of standard angle ($s1$) for each wavelength, (b) $D_{(s1,s2)}$ as a function of $s1$ for each wavelength divided by 415 nm band, (c) $D_{(s1,s2)}$ as a function of $s1$ at 321 nm divided by 415 nm, using the parameters of the maria (red), the highlands (blue), and all area (green), and (d) $D_{(s1,s2)}$ of the 321 nm (solid line) and 415 nm (dashed line) at the maria (red) and the highlands (blue). $s2 = 30^\circ$ for all plots. The parameters from $5^\circ S$ to $5^\circ N$, $0^\circ E$ to $360^\circ E$ were used to sample evenly across the range of phase angles.

259.76°E. Also, h_s is relatively high (0.09 to 0.12) along high-reflectance rays (highland areas), such as from Jackson crater (22.14°N, 196.70°E), Necho crater (5.10°S, 123.42°E), and Ohm crater (18.28°N, 246.36°E).

At poleward of $\sim 40^\circ$ latitude, b is systematically low (-0.026 in average), c is high ($+0.28$ in average), and h_s is low (about -0.035 in average) with higher random variations, relative to the equatorial region. These high-latitude trends are fitting artifacts likely related to the limited range of i and g in low values.

The regional trends of the five parameters (w , b , c , B_{SO} , and h_s) as a function of the seven wavelengths are shown in Figure 17. To minimize artifacts in b , c , and h_s at high latitudes, only $30^\circ S$ to $30^\circ N$ were used for this analysis. The extents of the three regions: the maria (red), highlands (blue), and all areas (green square) are illustrated in Figure 17f. Using the FeO abundance estimated with Clementine data [Lucey et al., 2000], we picked regions of $FeO > 16.0$ wt % as the maria, and regions of $FeO < 7.0$ wt % as the highlands.

The parameter w (Figure 17a) monotonically increases with wavelength in the maria and highlands, with the maria (red) being lower than the highlands (blue) as expected in the context of a compositional difference between the two terrains. In the maria, b is distinctly higher (thus lower in c) than the highlands (Figures 17b and 17c), except in the 321 nm band. This indicates that the backscattering is relatively weaker in the maria than the highlands in all wavelengths except 321 nm. Also in the maria, b slightly increases (thus c decreases) with wavelength from 360 to 689 nm, but considering the large error bars, the significance is low. The B_{SO} (Figure 17d) linearly decreases with wavelength in all regions, which is expected because B_{SO} is inversely proportional to w (equation (4)). This decreasing trend with wavelength is also reported in Hapke et al. [2012]. Note that the B_{SO} is above 1.0 due to ignoring CBOE [Hapke et al., 2012]. The h_s in the maria is lower than the highlands (Figures 16e and 17e red line) for all the wavelengths. Also h_s slightly decreases in the maria with wavelength, but the significance is low due to the large error bars.

3.5. Effect of Standard Angles on Normalized I/F

The plots of $D_{(s1,s2)}$ (n/F differences caused by the standard angle change, see section 2.4, equation (7)) as a function of standard angle ($s1$) show similar shapes for all wavelengths, but the slope gradually decreases with wavelength (Figure 18a). The $D_{(s1,s2)}$ for all wavelengths divided by the 415 nm band exhibits a

continuous decrease for $s1 < 30^\circ$ and then increase for $s1 > 30^\circ$ with wavelength (Figure 18b). The decreasing gradient of the phase curve as a function of wavelength is known as phase reddening [Gehrels et al., 1964]. The 321 and 689 nm bands show the largest difference at $g = 0^\circ$ (1.08 in 321 nm, 0.89 in 689 nm). For example, the ratio of 321/689 nm using the nI/F_{0° is 21.3% ($= 1.08/0.89 - 1$), larger in average than the same ratio using the nI/F_{30° .

The $D_{(s1,s2)}$ of the 321 nm band divided by the 415 nm band was plotted for the three regions (maria, highlands, and all; Figure 18c). The region "all" corresponds to the area within a narrow $\pm 5^\circ$ N equatorial area. The maria and the highland regions here correspond to the region of $FeO > 16.0$ wt % and $FeO < 7.0$ wt %, respectively (from FeO abundance map, [Lucey et al., 2000]), within $\pm 5^\circ$ N equatorial area. The maria (red) and highlands (blue) behave differently, particularly at $s1 < 30^\circ$. For example, the ratio of 321/415 nm for nI/F_{0° is 1.8% larger than the ratio using nI/F_{30° in the maria, whereas it is 5.9% larger in the highlands. In Figure 18d, the highlands 415 nm slope (blue dashed curve) is shallower and lower than the 321 nm (blue solid curve), while the maria 415 nm slope (red dashed curve) is steeper and overlaps the 321 nm (red solid curve), resulting in shallower, distinctive ratio curve (321/415 nm) for $s1 < 30^\circ$ in the maria (Figure 18c) relative to the highlands.

These regional comparisons show that the nI/F varies independently in the maria and highland units as the standard angle varies at lower values ($< 25^\circ$). This fact implies that for each geologic unit the influence of the standard angle on the nI/F can be different depending on each photometric property. However, in $s1 = 60^\circ$ (the standard angle used in this study) the offsets between the maria and highlands are negligible (from 0.3 to 0.6% for all wavelengths), at least within the $\pm 5^\circ$ N equatorial area.

4. Discussion: Interpretation of the Hapke Parameter Maps

Since all free parameters in the Hapke model have physical meanings, variations within the parameter maps relate to surface properties in a geologically meaningful manner. To obtain reliable parameters for such use, however, care must be taken to avoid mathematical couplings [Helfenstein, 1986; Mustard and Pieters, 1989] that cause the ill-posed problem (mathematically impossible to derive unique solution) [Baratoux et al., 2006]. Souchon et al. [2011] applied certain simplifications to the Hapke model to reduce the number of free parameters. For the model fitting they employed an evolutionary algorithm [Cord et al., 2003] that can find a global minimum and successfully extracted the link between b, c (equation (A3)) and the properties of the natural samples. Hapke et al. [2012] also applied significant simplifications of the Hapke model and examined the properties of the opposition effect as a function of wavelength from WAC observations. Our parameter maps returned valid photometric corrections for almost all the tiles (see section 3.2), which implies that the model and parameters are accurately replicating the observed photometric behaviors. We note that in the map of b, c , and h_s (Figures 16b, 16c, and 16e) for latitudes above $\pm 40^\circ$, abnormal tiles are correlated between the three parameter maps. Thus, in this region the mathematical coupling between h_s and b, c may have occurred, again likely due to the systematic decrease in i and g ranges for high-latitude tiles.

The simplification we applied to the Hapke model influences the absolute values of the calculated parameters. Ignoring the porosity factor results in a higher w than the actual value, as well as exaggerating the multiple scattering effect (equation (A5)) at high i and e , leading to a smaller dependence on the shadow effect thus a smaller $\bar{\ell}_p$. Ignoring the CBOE results in B_{50} values that are greater than 1.0, which is a theoretical upper limit, probably because the SHOE accounts for both the contributions of SHOE and CBOE as described in Hapke et al. [2012].

Calculation of c using the hockey stick relation (equation (2)) is based on laboratory measurements using a variety of samples [Hapke, 2012b]. When we independently calculate the b and c of the Henyey-Greenstein phase function (equation (A3)) for the equatorial tiles (within $\pm 3^\circ$), the values are clustered around the "hockey stick" curve (equation (2)) on a plot of b versus c (Figure 19), implying that the WAC data generally follow the predicted b and c trend derived from the laboratory samples. However, the center of the highest density spot varies with wavelength and is slightly offset from the equation (2) curve (Figure 19), particularly in 566 nm and longer wavelengths. Such wavelength dependence of b, c was also recognized in Figures 17b and 17c. Mustard and Pieters [1989] using a two-term Legendre polynomial (instead of Henyey-Greenstein phase function) reported some link between the surface mineralogies and the

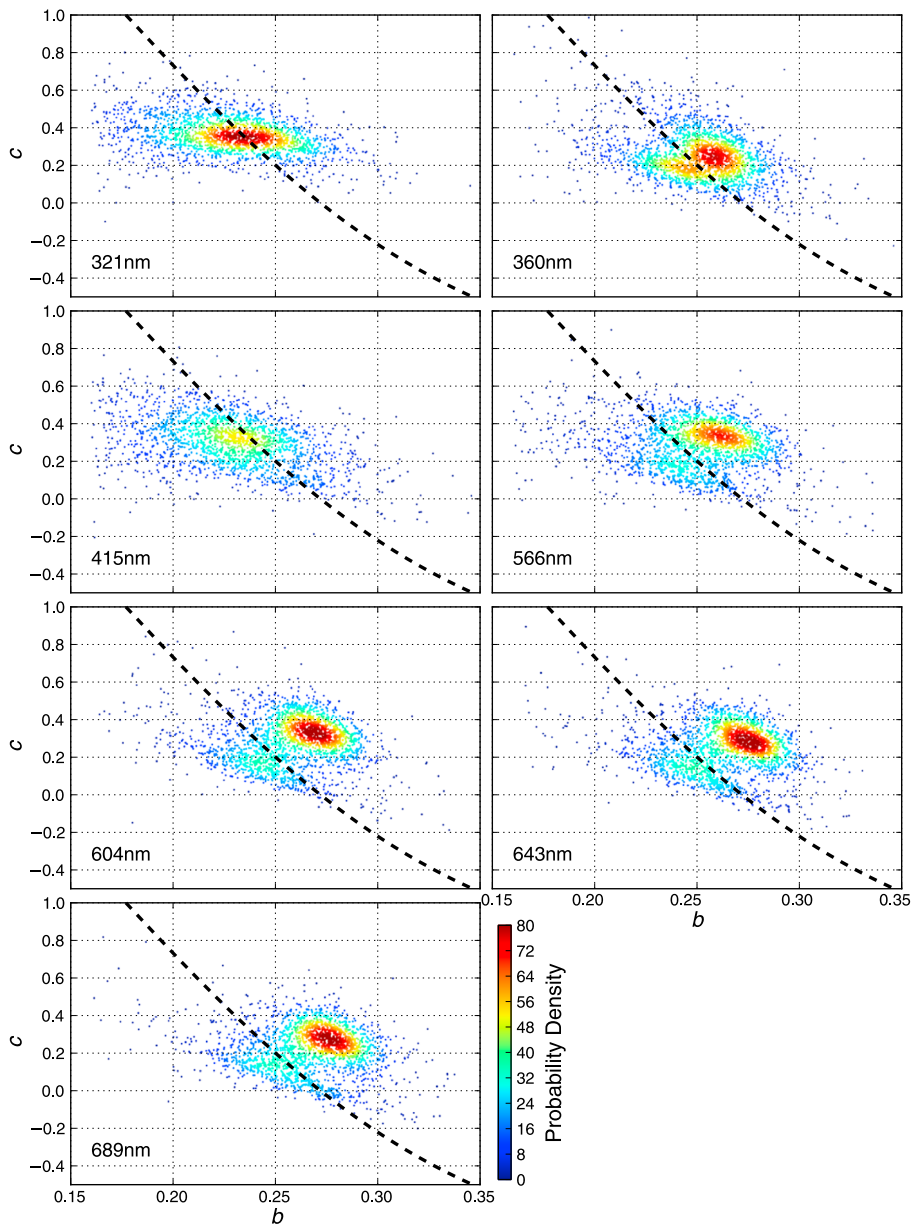


Figure 19. Plots of Henyey-Greenstein phase function parameters b , c (independently calculated without using equation (2)) for each tile inside 3°S to 3°N latitude, 0° to 360°E longitude, in all the wavelengths. The dot indicates the b , c values from one tile. The color represents a two-dimensional probability density using Gaussian kernel-density estimation. The dashed line is equation (2) from hockey stick relation [Hapke, 2012b].

phase curve change as a function of the wavelength. Further investigations of the phase curve at various wavelength will help to understand the detailed behavior of b, c that improves the accuracy of c interpolation.

The $\bar{\theta}_p$ computed for the equatorial area is not spatially correlated with geologic context (see section 2.3), while following observations related to surface roughness have suggested such spatial correlations should occur. The rock abundance by Earth-based radar observation (few-centimeter scale, [Campbell *et al.*, 2010]) and the rock concentration detected by Diviner (~ 1 m in diameter, [Bandfield *et al.*, 2011]) are higher on the mare basalt than in the highlands. The median differential slope derived by Lunar Orbiter Laser Altimeter (LOLA; ~ 17 m effective baseline, [Rosenburg *et al.*, 2011]) is higher in the highlands than the mare. The scale that dominates the photometric roughness is considered as at least millimeter range, possibly $\sim 100 \mu\text{m}$ scale for lunar regolith [Shepard and Campbell, 1998; Helfenstein and Shepard, 1999; Cord *et al.*, 2003], which

is much smaller than the target roughness scale in Diviner, LOLA, and the radar observations. Probably due to this distinctly small sensible roughness scale, the $\bar{\theta}_p$ did not show any clear spatial variation. The histograms of $\bar{\theta}_p$ in Figure 8 exhibit offsets (about $\pm 1.5^\circ$) in the peak values across the wavelength, particularly in the 360 nm. *Cord et al.* [2003] reported nearly constant but marginally decreasing roughness parameter with wavelength ($\sim 1^\circ$ decrease from 600 to 780 nm). Our result does not show clear decreasing trend. Thus, the minor quality deviation in the radiometric calibration at each filter could be responsible for this random shifts in the $\bar{\theta}_p$ histograms.

The physical validity of estimating B_{S0} based on w and $S(0)$ is unknown, but their correlation is clear (Figure 9). The decreasing trend of B_{S0} with wavelength shown in Figure 17d is consistent with *Hapke et al.* [2012], but our B_{S0} is larger, about +0.8 in maria and about +0.4 in the highlands. The data set used in *Hapke et al.* [2012] was acquired from a highland region, north of the Orientale basin, which likely accounts for the closer B_{S0} agreement in the highlands to their values. In their model, however, more simplifications are applied to the original form of Hapke model, including the use of a single-lobed Henyey-Greenstein phase function, and exclusion of the shadow effect. Deriving another set of parameter maps employing their simplified function would allow a direct comparison of the B_{S0} with their values.

The h_S controls the gradient (or width) of the SHOE function which is significant at about $g < 40^\circ$. At high latitudes where g is mostly limited to values $> 40^\circ$, the contribution of SHOE becomes almost negligible, thus a reliable h_S value is hard to derive. Considering that B_{S0} is calculated based on values of w , b , and c (equation (4)), all the uncertainties of SHOE accumulate on h_S . Thus, the anomalous h_S values at high latitudes in Figure 16e likely reflects the small SHOE contributions, increasing the h_S uncertainties toward the pole. The calculations of b and c are also sensitive to the g range. The cutoff of $g \geq 97^\circ$ (see section 2.2) in addition to the increasing lower limit of g toward the pole results in systematically small ranges of g at high latitudes and increases the uncertainties of b and c above $\pm 40^\circ$ latitudes. Even though the derived parameters at high latitudes are still valid and return optimal photometric normalization, the physical meaning of those parameters is hard to interpret. Therefore, we interpret our parameter maps only between 40°S to 40°N latitude in the following discussion.

In the all three regions ("Maria," "Highlands," and "All area") in Figure 17a, w increases monotonically with wavelength. Within the WAC's wavelength range (321–689 nm), the spectra of mature lunar soils are known to monotonically increase with wavelength in bulk samples [*McKay et al.*, 1991; *Isaacson et al.*, 2011]. Since all three regions are dominantly mature surface (average optical maturity parameter [*Lucey et al.*, 2000] is 0.172 for "Maria," 0.178 for "Highlands," 0.175 for "All area," and the immature surface is about ~0.3), the monotonic increase of w (and nI/F as well) with wavelength is an expected result.

Based on the definitions of the Hapke parameters and their known links to physical properties [*Mustard and Pieters*, 1989; *Clark*, 1995; *McGuire and Hapke*, 1995; *Lucey*, 1998; *Lawrence and Lucey*, 2007; *Denevi et al.*, 2008; *Souchon et al.*, 2011], and taking all the possible calculation errors into account, what can we learn about lunar surface properties from the parameter maps? A key result is the high b and low c for the maria relative to the highlands (Figures 17b and 17c), indicating decreased backscattering in the maria relative to the highlands. Laboratory measurements of the Apollo soils [*Johnson et al.*, 2013] reveal lower c for the Apollo 11 soil (-0.39 ± 0.02 at < 689 nm wavelength, mare materials) relative to the Apollo 16 soil (-0.29 ± 0.04 , highland materials). Note that these b and c values are already converted from the version in *Johnson et al.* [2013] ranging $0 \leq b \leq 1$ and $0 \leq c \leq 1$ to the version used in this study ranging $0 \leq b \leq 1$ and $-1 \leq c \leq 1$. For both mare and highland soil samples, the b and c values plot close to the hockey stick field (Figure 20, blue curve). The c is lower for the mare soil relative to the highland soil which is also seen in the parameter maps, though the values are different. For both Apollo 11 and 16 soils the c is lower than 0, indicating the forward scattering dominant regime. The difference of c between the mare and the highlands for the Apollo soils is smaller than our parameter map values (0.14 and 0.53 for the Apollo 11 and 16 sites in 643 nm). Also, the b for the Apollo soils (0.34 and 0.33 for the Apollo 11 and 16 sites, < 689 nm) are higher than our parameter map values (0.21 and 0.25 for the Apollo 11 and 16 sites in 643 nm). We attribute these differences to the model simplifications employed and the parameter calculation algorithms. Additionally, physical difference between the undisturbed uppermost regolith layer and the stirred sample surface likely also results in changes to photometric properties.

Several studies suggest a link between the b, c values and the physical properties of surface materials. *McGuire and Hapke* [1995] examined the effects of characteristic grain properties on the phase function

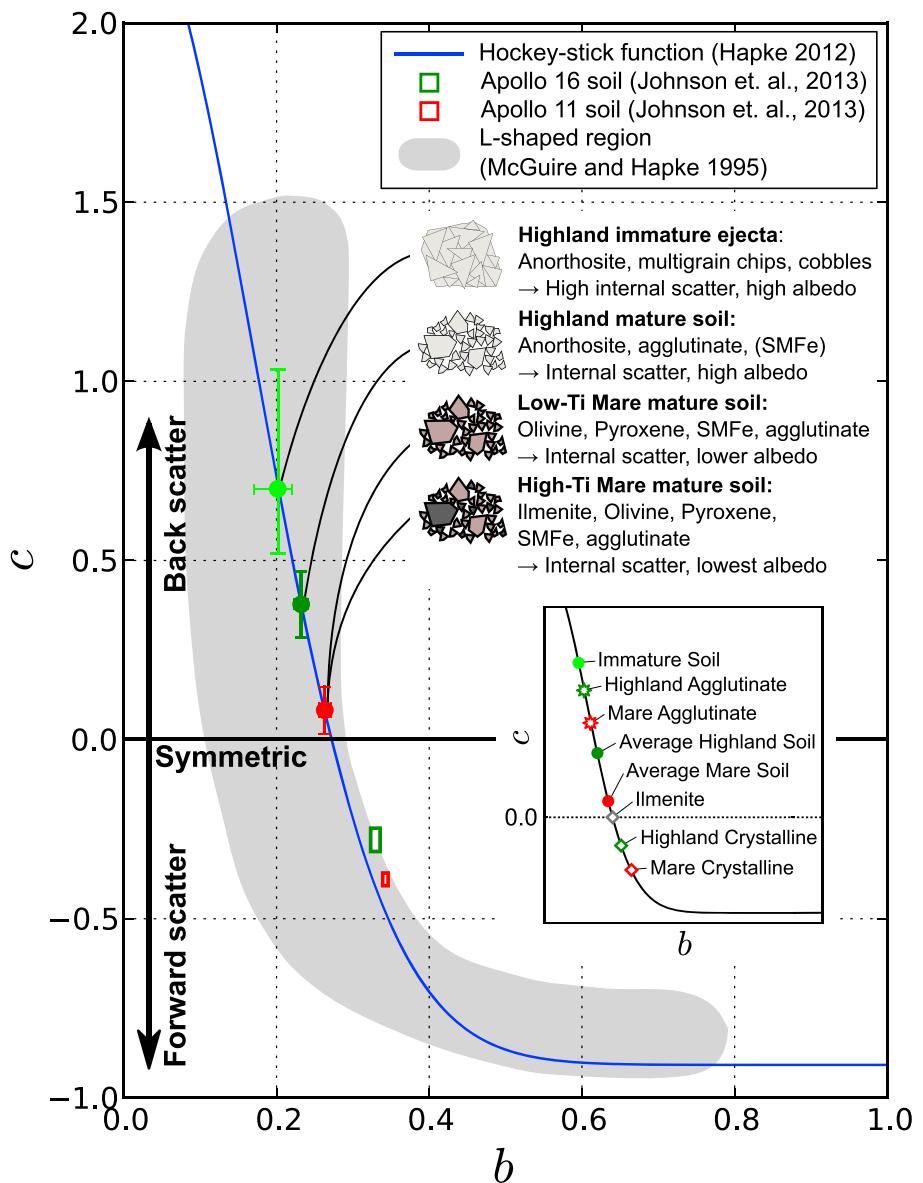


Figure 20. The typical values of b and c (Henyey-Greenstein phase function parameters) for the mature mare (low and high Ti content), the mature highland, and the immature highland ejecta in 643 nm band parameter maps. Red and green denote the values in the maria and the highland regions, respectively. The blue curve indicates equation (2) (hockey stick relation, [Hapke, 2012b]). Schematic diagram inserted in the lower right illustrates qualitative model of b and c values for crystalline and agglutinates in the mare and the highland.

using well-controlled artificial materials (metallic iron, resin, glass with/without TiO_2 submicron particle inclusions). They found that the phase curve (expressed by b, c) depends on grain shape, surface roughness, internal scattering (caused by inclusions, pores, and structural complexities inside grains), and internal absorption (albedo). Increased surface roughness, shape irregularity, and internal scattering of grains result in increased backscattering with smoother phase curves. Likewise, a decrease in albedo results in flatter and nearly symmetric scatter due to strong absorption that prevents internal scattering (forward or backward). Since lunar regolith contains about 50–60 vol % agglutinates [McKay et al., 1991], they must significantly affect the net scattering properties. The complicated surface and internal structure of agglutinates cause a high density of internal scattering that generally results in strong backscattering (high c). However, the low albedo of agglutinates (due to SMFe, ilmenite, and other opaque species) decreases the backscattering contribution resulting in a more symmetric scattering pattern. Opaque ilmenite grains (assuming

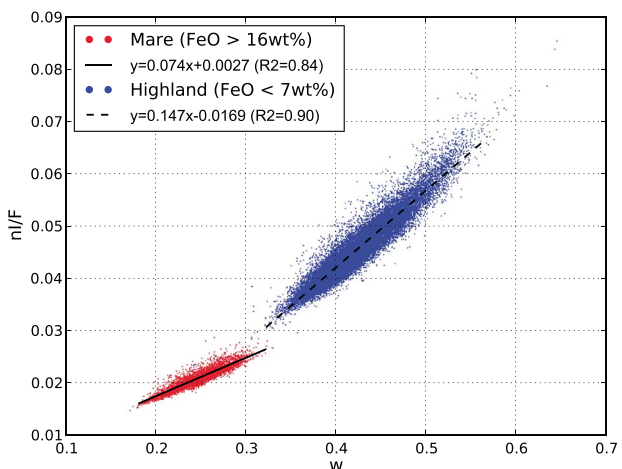


Figure 21. Plots of w versus nl/F (643 nm band) in the mare and the highland for 70°S to 70°N , 0° to 360°E . Dot represents the value of w and a median of nl/F (normalized by $i = g = 60^{\circ}$, $e = 0^{\circ}$) within each tile. FeO abundance [Lucey et al., 2000] was used to define the mare area (> 16.0 wt %) and the highland area (< 7.0 wt %).

amounts of SMFe. Thus, the phase function is backscattering, resulting in higher c (lower b) (see Figure 20). The mature mare regolith, in turn, includes a higher content of ilmenite and SMFe [McKay et al., 1991], which decrease the albedo. Some of the SMFe are in the surface coatings on the silicate grains, but more are in the interior of the agglutinates, so that agglutinate backscattering is reduced more than silicate grain forward scattering, resulting in lower c (higher b). Maria with high concentration of Ti (e.g., Mare Tranquillitatis and Oceanus Procellarum) and those with low Ti concentrations (e.g., Mare Serenitatis and Crisium), however, do not show a clear difference in b and c values (Figures 16b and 16c) despite the clear albedo contrast (in 643 nm band). Ilmenite lowers the albedo of backscattering agglutinates and also decreases the fraction of forward scattering silicates (see Figure 20), while the SMFe in the grain coatings and interior of the agglutinates does not change. As a net effect, high/low Ti will have similar b, c values. In the 321 nm band, the b, c values for the maria and the highlands are roughly in a same range within the error bars (Figures 17b and 17c). This may be because the shorter wavelength light is more readily absorbed inside grains than longer wavelengths by the SMFe, even in highland materials, resulting in phase curves that are insensitive to the compositional contrast (mare versus highlands).

Anomalously low b (0.20 ± 0.02) and high c (0.7 ± 0.3) areas, indicating strong backscattering properties, are colocated with relatively young craters (e.g., Necho, King, and Vavilov), particularly within the cavity and vicinity of the crater rim. The ejecta deposits have slightly higher c ($\sim 10\%$) relative to the background, which faints with the distance from the crater rim without obvious distal edge. Immature highland outcrops along the crater walls and the ejecta expose fresh anorthosite in multigrain chips, cobbles, and rocks (free from SMFe), which are optically thick and have high albedos with a high density of internal scatters. Thus, such fresh anorthosite rocks should exhibit strong backscattering. As the ejecta travels farther from the impact center, there is a greater chance of incorporating mature regolith (due to local mixing as the thin blanket of ejecta gardens the target) that decreases the net fraction of backscattering from ejecta.

Relatively high values of h_s also occur for the highland fresh ejecta (Figure 16e). The typical contrast in h_s between the highlands (higher) and the maria (lower) was revealed as well (Figures 16e and 17e). However, due to the lack of comprehensive laboratory studies of the relationship between h_s and sample properties, the interpretation of h_s based on ground truth is problematic. Theoretically, the h_s is related to the filling factor ϕ (= 1 – porosity) and grain size distribution [Hapke, 2012a] of the surface soil. The porosity of mature regolith could be nearly uniform all over the Moon because it is controlled by micrometeorite impacts. Mineral grains (i.e., ilmenite versus silicate minerals) may comminute at different rates, which might cause a different grain size distribution in the maria than in the highlands, resulting in the typically lower h_s for the maria relative to the highlands. Compared to the mature regolith, the fresh crater ejecta could contain particles large enough to decrease v (the slope of particle size distribution in a power law form, [Hapke,

more-or-less smooth surface texture) scatter approximately symmetrically, similar to smooth-surfaced metal [McGuire and Hapke, 1995]. Relatively transparent silicate grains are forward scattering. However, silicate rocks, consisting of numerous crystals, are optically thick due to long internal path lengths (and thus increased chance of internal absorption) and rough interfaces between crystals, and thus tend to be backscattering.

The b, c parameter maps (Figures 16b and 16c) show a marked contrast between the maria (lower c : 0.08 ± 0.06 , higher b : 0.26 ± 0.01) and the highlands (higher c : 0.38 ± 0.09 , lower b : 0.23 ± 0.01). The mature highland regolith includes agglutinates formed from relatively high-albedo materials (e.g., anorthosite with little ilmenite) and relatively small

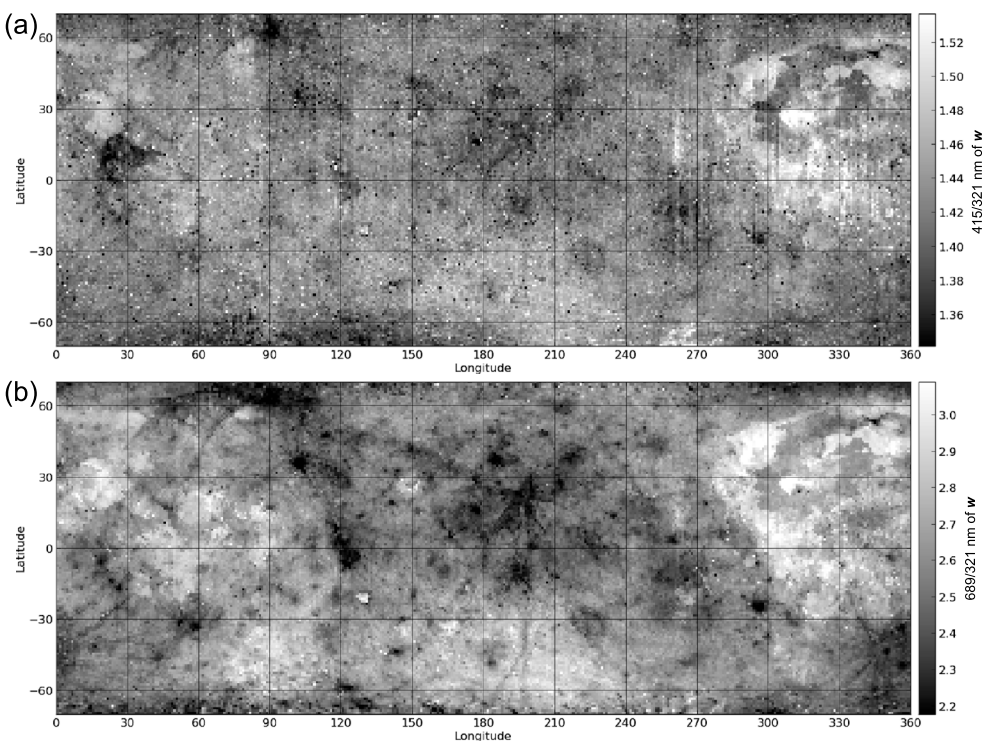


Figure 22. The ratio of parameter map w in (a) 415/321 nm bands and (b) 689/321 nm bands.

2012a]), which would increase h_s for the immature ejecta deposits observed in the highlands. The mature regolith, the ultimate product of comminution or grinding by micrometeorite impacts, is expected to be approximately $v = 4$ that derives $h_s = 0.061$ [McKay *et al.*, 1974; Hapke, 2012a], thus $v < 1.4$ theoretically results in higher h_s than the mature regolith. On the other hand, fresh craters in the mare do not show relatively higher h_s as seen in the highland. The reason is unknown, but it might be related to different physical strength (as a target property of the impacts) between the mare and the highland.

The cause of the decreasing trend in h_s with wavelength in the maria (Figure 17e) is currently unresolved. Laboratory measurements to confirm the physical meaning of h_s could test if this trend is real and shed light on the root cause.

Reflectance is dominantly influenced by photometric angles and physical state properties (e.g., surface roughness, grain size, grain shape, opacity, and porosity) [Kamei *et al.*, 1999; Piatek *et al.*, 2004; Näränen *et al.*, 2004; Hapke, 2008; Souchon *et al.*, 2011; Shepard and Helfenstein, 2011] in addition to the composition and spectral absorption coefficient of each mineral. The nl/F is still dependent on the standard angles (see section 3.5) and the physical state properties, thus not purely controlled by compositional variability like w . The plot of w and nl/F in 643 nm (Figure 21) is an example, revealing their strong linear correlation but the different trends between the maria and the highlands, due to the different photometric behaviors in these two geologic units. In our standard angles of nl/F ($i = g = 60^\circ$, $e = 0^\circ$), the opposition surge effects are negligible and the shadow effects are fixed by the constant $\bar{\theta}_p$. Thus, the dominant effect on the nl/F is w and the phase curve (controlled by b and c). The low c in the maria relative to the highlands (Figure 16c) indicates relatively lower phase curve at $g = 60^\circ$ due to the smaller backscatter in the maria. The shallower slope of the maria in w versus nl/F trend (Figure 21) relative to the highlands is likely due to the lower phase curve at $g = 60^\circ$ (acts as a smaller multiplier in addition to w).

Key spectral ratios of w (415/321 nm; Figure 22a, 689/321 nm; Figure 22b) are grossly similar but not identical to the corresponding simple nl/F ratios (Figures 11b and 11c), implying the presence of physical state property effects in the nl/F . The w derived in this study is not dependent on the standard angles and most physical state properties (except porosity, see section 2.3). Thus, spectral analysis using w may improve the accuracy of mineral identification through spectroscopic methods, similar to the techniques described in

Clark [1995], Lucey [1998], Lawrence and Lucey [2007], and Denevi *et al.* [2008]. Unlike the previous photometric data sets, the extensive repeated observations with varying photometric geometries acquired by the WAC enables spatially resolved spectral analysis using w on a near-global scale.

The links between the Hapke parameters and several physical state properties (e.g., the surface roughness, grain size, and porosity) were examined with laboratory experiments and computer simulations [Cord *et al.*, 2003; Piatek *et al.*, 2004; Shkuratov *et al.*, 2005; Shepard and Helfenstein, 2007], but clear causal correlations are not yet unequivocal. Also, opposition effects (B_{C0} , h_C , B_{S0} , h_S) in relation to the physical properties of the reflecting materials are still poorly understood [Hapke *et al.*, 2012]. Comprehensive laboratory experiments improving the knowledge and techniques to retrieve the physical state properties from the photometric parameters will further extend the potential of the WAC photometric observations to unravel the complexity of lunar surface materials.

5. Summary and Conclusion

We derived spatially resolved (1° by 1°) Hapke parameters by a tile-by-tile method utilizing an extensive multispectral multitemporal LROC WAC near-global data set for the photometric normalization. From about 66,000 WAC multispectral images acquired from February 2010 to October 2011, we computed latitude, longitude, incidence (i), emission (e), and phase (g) angles for each image pixel based on WAC stereo DTM (GLD100, 100 m/pixel). For the efficient parameter calculation that achieves higher accuracy and saves significant computation resources, we applied albedo filtering and angle binning, to minimize data scatter by reducing the albedo variation within a tile and to reduce the number of data points about 40 times. Since the accurate determination of all nine parameters (w , b , c , B_{C0} , h_C , B_{S0} , h_S , $\bar{\theta}_p$, ϕ) of Hapke bidirectional reflectance function [Hapke, 2012a] by the model fitting is mathematically difficult, we set CBOE (coherent backscatter opposition effect) and K (porosity effect) to 1.0 ($B_{C0} = \phi = 0$) to simplify the model. Also, the c was derived by b using the empirical function based on the hockey stick relation [Hapke, 2012b]. Then we derived $\bar{\theta}_p$ (a constant value; 23.4) and B_{S0} (linear interpolation using w , b , and c) from an equatorial band (3°S to 3°N). The remaining three free parameters (w , b , and h_S) were calculated by least-squares fitting with 30 different starting parameter sets to minimize the starting value dependency. The photometrically normalized near-global (0°E to 360°E , 70°S to 70°N) seven band mosaics, given by the median of normalized (standard angles $i = g = 60^\circ$, $e = 0^\circ$ instead of the traditional angles $i = g = 30^\circ$, $e = 0^\circ$) radiance factor (nl/F) from 21 months of the WAC observations, do not exhibit significant color artifacts with latitude or along the tile boundaries. The fitting accuracy for all tiles is 0.96 (median) ± 0.07 (standard deviation) in R^2 and 0.041 (median) ± 0.009 (standard deviation) in σ_m . Both R^2 and σ_m indicate decreasing accuracy toward the pole because i , g dominantly increase and their variations at lower values decrease toward the pole. The relatively larger fitting residuals within highland terrain (higher σ_m) relative to the maria (lower σ_m) are due to the imperfect calculations of i , e , and g at small-scale topographic undulations unresolved by the WAC DTM, which occur more often within the hilly highlands. The offsets along the tile boundaries are 0.26% in median (A_m) and 0.40% in standard deviation (A_s) relative to each nl/F . The increased offsets beyond 60° latitudes (up to twice larger relative to the equator) reflect the limited range of i , g at high latitudes, resulting in increased fitting uncertainties and random variations in the parameter maps. The influence of standard angle ($s1$) change on the nl/F revealed the phase reddening, which causes 21.3% of offsets between $s1 = 0^\circ$ and 30° in 321/689 nm ratio values. Also, the nl/F change with standard angle between the maria and the highlands is different, for example, in the maria the 321/415 nm ratio value at $s1 = 5^\circ$ is 1.8% higher than the ratio at $s1 = 30^\circ$ whereas 5.9% higher (in the same comparison) in the highlands. The Hapke parameter maps derived by our tile-by-tile method revealed regional variations in photometric properties of the lunar surface. The w (single scattering albedo) has a clear correlation with the nl/F . But the ratio of w maps (e.g., 415/321 and 689/321 nm bands) represent different spatial variation from the ratio of nl/F , highlighting the difference of surface albedo and the normalized reflectance. The b, c (Henyey-Greenstein phase function parameter) values suggest that the highland regolith is dominantly backscattering due to the abundance of agglutinates formed from high-albedo silicates. The maria represent decreased backscattering relative to the highlands (except within the 321 nm band) likely due to higher content of SMFe and opaque minerals in the interiors of the agglutinates. The h_S (angular width of SHOE) has lower values for mature mare materials relative to mature highland materials. Immature crater ejecta within the highlands (e.g., Jackson, Necho, and Ohm crater) exhibit relatively higher h_S values than the mature material. These variations in h_S are possibly

caused by variations in grain size distributions. Better knowledge of the link between the parameters and the physical properties of actual materials is necessary for the photometric analysis of lunar surface. A comprehensive study of Hapke parameters using various samples in laboratory experiments could provide such crucial knowledge and may elucidate many of the issues raised by this work.

Appendix A: Mathematical Expression of Hapke Function

In this model, radiance factor I/F [Hapke, 2012a] is written as

$$I/F = LS(i_e, e_e)K \frac{w}{4} [p(g)(1 + B_{S0}B_S(g)) + M(i_e, e_e)] [1 + B_{C0}B_C(g)]S(i, e, \psi) \quad (A1)$$

where LS is the Lommel-Seeliger function, i_e and e_e are effective angle of incidence and emission respectively, K is porosity factor, w is single scattering albedo, $p(g)$ is phase function, B_{S0} is amplitude of Shadow Hiding Opposition Effect (SHOE), $B_S(g)$ is SHOE function, $M(i_e, e_e)$ is Isotropic Multiple-Scattering Approximation (IMSA) [Hapke, 1981, 1999], B_{C0} is amplitude of Coherent Backscatter Opposition Effect (CBOE), $B_C(g)$ is CBOE function, $S(i, e, \psi)$ is shadowing function, and ψ is azimuthal angle between the planes of incidence and emergence (Figure 2). The Lommel-Seeliger function (LS) is given by

$$LS(i_e, e_e) = \frac{\cos(i_e)}{\cos(i_e) + \cos(e_e)} \quad (A2)$$

For the phase function $p(g)$, we employed Henyey-Greenstein double-lobed single particle phase function,

$$p(g) = \frac{1+c}{2} \frac{1-b^2}{(1-2b\cos(g)+b^2)^{3/2}} + \frac{1-c}{2} \frac{1-b^2}{(1+2b\cos(g)+b^2)^{3/2}} \quad (A3)$$

where b ($0 \leq b \leq 1$) is the shape-controlling parameter, and c ($-1 \leq c \leq 1$) is the relative strength of backward and forward lobes. The SHOE function $B_S(g)$ is given by

$$B_S(g) = 1/[1 + \tan(g/2)/h_S] \quad (A4)$$

where h_S is the angular width parameter of SHOE. The IMSA function $M(i_e, e_e)$ is given by

$$M(i_e, e_e) = H\left(\frac{\cos(i_e)}{K}, w\right)H\left(\frac{\cos(e_e)}{K}, w\right) - 1 \quad (A5)$$

where $H(x,w)$ is Ambartsumian-Chandrasekhar H function, which is approximated by

$$H(x,w) \approx \left\{ 1 - wx \left[r_0 + \frac{1-2r_0x}{2} \ln\left(\frac{1+x}{x}\right) \right] \right\}^{-1} \quad (A6)$$

where r_0 is diffusive reflectance, given by

$$r_0 = \frac{1 - \sqrt{1-w}}{1 + \sqrt{1-w}} \quad (A7)$$

The CBOE function $B_C(g)$ is given by

$$B_C(g) = \frac{1 + \frac{1 - \exp[-\tan(g/2)/h_C]}{\tan(g/2)/h_C}}{2 [1 + \tan(g/2)/h_C]^2} \quad (A8)$$

where h_C is angular width of CBOE.

The porosity factor K is

$$K = \frac{-\ln(1 - 1.209\phi^{2/3})}{1.209\phi^{2/3}} \quad (A9)$$

where ϕ is filling factor that is equivalent to 1 – porosity. The K monotonically increases with the filling factor ϕ (= 1 – porosity).

The i_e , e_e , and the shadowing function $S(i, e, \psi)$ are the functions of $\bar{\theta}_p$, the effective value of the photometric roughness. When $i \leq e$, $S(i, e, \psi)$ is

$$S(i, e, \psi) = \frac{\mu_e}{\eta(i)} \frac{\mu_0}{1 - f(\psi) + f(\psi)\chi(\bar{\theta}_p)[\mu_0/\eta(i)]} \quad (\text{A10})$$

where the cosine of effective angle of incidence μ_{0e} and the cosine of effective angle of emission μ_e are

$$\mu_{0e} = \cos(i_e) = \chi(\bar{\theta}_p) \left[\cos(i) + \sin(i) \tan(\bar{\theta}_p) \frac{\cos(\psi)E_2(e) + \sin^2(\psi/2)E_2(i)}{2 - E_1(e) - (\psi/\pi)E_1(i)} \right] \quad (\text{A11})$$

$$\mu_e = \cos(e_e) = \chi(\bar{\theta}_p) \left[\cos(e) + \sin(e) \tan(\bar{\theta}_p) \frac{E_2(e) - \sin^2(\psi/2)E_2(i)}{2 - E_1(e) - (\psi/\pi)E_1(i)} \right] \quad (\text{A12})$$

When $e \leq i$, $S(i, e, \psi)$ is

$$S(i, e, \psi) = \frac{\mu_e}{\eta(i)} \frac{\mu_0}{1 - f(\psi) + f(\psi)\chi(\bar{\theta}_p)[\mu/\eta(e)]} \quad (\text{A13})$$

where μ_{0e} and μ_e are

$$\mu_{0e} = \cos(i_e) = \chi(\bar{\theta}_p) \left[\cos(i) + \sin(i) \tan(\bar{\theta}_p) \frac{E_2(i) - \sin^2(\psi/2)E_2(e)}{2 - E_1(i) - (\psi/\pi)E_1(e)} \right] \quad (\text{A14})$$

$$\mu_e = \cos(e_e) = \chi(\bar{\theta}_p) \left[\cos(e) + \sin(e) \tan(\bar{\theta}_p) \frac{\cos(\psi)E_2(i) + \sin^2(\psi/2)E_2(e)}{2 - E_1(i) - (\psi/\pi)E_1(e)} \right] \quad (\text{A15})$$

where $\chi(\bar{\theta}_p)$ is

$$\chi(\bar{\theta}_p) = 1/[1 + \pi \tan^2(\bar{\theta}_p)]^{1/2} \quad (\text{A16})$$

and $\eta(y)$ is, (y corresponds to i or e)

$$\eta(y) = \chi(\bar{\theta}_p) \left[\cos(y) + \sin(y) \tan(\bar{\theta}_p) \frac{E_2(y)}{2 - E_1(y)} \right] \quad (\text{A17})$$

where E_1 and E_2 are, (y corresponds to i or e)

$$E_1(y) = \exp \left[-\frac{2}{\pi} \cot(\bar{\theta}_p) \cot(y) \right] \quad (\text{A18})$$

$$E_2(y) = \exp \left[-\frac{1}{\pi} \cot^2(\bar{\theta}_p) \cot^2(y) \right] \quad (\text{A19})$$

$f(\psi)$ is given by

$$f(\psi) = \exp \left[-2 \tan \left(\frac{\psi}{2} \right) \right] \quad (\text{A20})$$

ψ , the azimuthal angle, is given by

$$\cos(g) = \cos(e) \cos(i) + \sin(e) \sin(i) \cos(\psi) \quad (\text{A21})$$

Thus, it can be written as

$$\psi = \arccos \left[\frac{\cos(g) - \cos(e) \cos(i)}{\sin(e) \sin(i)} \right] \quad (\text{A22})$$

Appendix B: Delta-v Burn Zone

The LRO orbit drifts from the ideal 50 km circular orbit to a 35 by 65 km orbit in 1 month, requiring a monthly burn to recircularize the orbit. During the burn, the instruments are disabled. The burn always takes place near the 90°W to 90°E plane to ensure continuous communication with the spacecraft. Since the WAC is pointing off nadir during the burns, there are significantly fewer observations at these longitudes.

Acknowledgments

This work was supported by the National Aeronautics and Space Administration Lunar Reconnaissance Orbiter Project. This research utilizes the USGS Integrated Software for Imagers and Spectrometers (ISIS). We wish to thank our colleagues, Samuel Lawrence, Prasun Mahanti, and LROC science teams, for constructive discussions about lunar surface materials and advices with WAC image processing.

References

- Akimov, L. A. (1975), Influence of mesorelief on the brightness distribution over a planetary disk, *Sov. Astron.*, 19(3), 1829–1841.
- Anderson, J. A., S. C. Sides, D. L. Soltesz, T. L. Sucharski, and K. J. Becker (2004), Modernization of the integrated software for imagers and spectrometers, Abstract 2039, paper presented at 35th Lunar and Planetary Science Conference, March 15–19, 2004, League City, Tex.
- Bandfield, J. L., R. R. Ghent, A. R. Vasavada, D. A. Paige, S. J. Lawrence, and M. S. Robinson (2011), Lunar surface rock abundance and regolith fines temperatures derived from LRO Diviner Radiometer data, *J. Geophys. Res.*, 116, E00H02, doi:10.1029/2011JE003866.
- Baratoux, D., P. C. Pinet, V. G. Kaydash, Y. Shkuratov, Y. Daydou, S. Besse, A. Jehl, and S. Chevrel (2006), The derivation of Hapke parameters using multi-angular observations from orbit and laboratory: An ill-posed problem, Abstract 1340, paper presented at 37th Annual Lunar and Planetary Science Conference, March 13–17, 2006, League City, Tex.
- Besse, S., J. Sunshine, M. Staid, J. Boardman, C. Pieters, P. Guasqui, E. Malaret, S. McLaughlin, Y. Yokota, and J.-Y. Li (2013), A visible and near-infrared photometric correction for Moon Mineralogy Mapper (M3), *Icarus*, 222(1), 229–242, doi:10.1016/j.icarus.2012.10.036.
- Borel, C., S. Gerstl, and B. Powers (1991), The radiosity method in optical remote sensing of structured 3-D surfaces, *Remote Sens. Environ.*, 36, 13–44.
- Boyd, A. K., M. S. Robinson, and H. Sato (2012), Lunar Reconnaissance Orbiter Wide Angle Camera photometry: An empirical solution, Abstract 2795 paper presented at 43rd Lunar and Planetary Science Conference, held March 19–23, 2012 at The Woodlands, Tex.
- Campbell, B. a., L. M. Carter, D. B. Campbell, M. Nolan, J. Chandler, R. R. Ghent, B. Ray Hawke, R. F. Anderson, and K. Wells (2010), Earth-based 12.6-cm wavelength radar mapping of the Moon: New views of impact melt distribution and mare physical properties, *Icarus*, 208(2), 565–573, doi:10.1016/j.icarus.2010.03.011.
- Clark, B. E. (1995), Spectral mixing models of S-type asteroids, *J. Geophys. Res.*, 100(E7), 14,443–14,456.
- Coutis, E., M. Craig, L. Kaletzke, K. McCormack, and L. Stewart (2006), HOSERLab: A new planetary spectrophotometer facility, Lunar Planet Science, XXXVII, Abstract 2121 paper presented at 37th Annual Lunar and Planetary Science Conference, March 13–17, 2006, League City, Tex.
- Coutis, E. A., K. A. Mccormack, J. F. Bell III, A. R. Hendrix, D. T. Bailey, M. A. Craig, S. A. Mertzman, M. S. Robinson, and M. A. Riner (2008), Ultraviolet spectral reflectance properties of common planetary minerals, *Icarus*, 197(1), 321–347, doi:10.1016/j.icarus.2008.04.018.
- Cord, A. M., P. C. Pinet, Y. Daydou, and S. D. Chevrel (2003), Planetary regolith surface analogs:, *Icarus*, 165(2), 414–427, doi:10.1016/S0019-1035(03)00204-5.
- Denevi, B. W., P. G. Lucey, and S. B. Sherman (2008), Radiative transfer modeling of near-infrared spectra of lunar mare soils: Theory and measurement, *J. Geophys. Res.*, 113, E02003, doi:10.1029/2007JE002929.
- Douté, S., and B. Schmitt (1998), A multilayer bidirectional reflectance model for the analysis of planetary surface hyperspectral images at visible and near-infrared wavelengths, *J. Geophys. Res.*, 103(98), 31,367–31,389.
- Fischer, E. M., and C. M. Pieters (1996), Composition and exposure age of the Apollo 16 Cayley and Descartes regions from Clementine data: Normalizing the optical effects of space weathering, *J. Geophys. Res.*, 101(95), 2225–2234.
- Fischer, E. M., C. M. Pieters, and S. F. Pratt (1994), Modeling the space weathering-induced optical alteration of lunar soils: First results, Abstracts 371 paper presented at 25th Lunar and Planetary Science Conference, held in Houston, TX, 14–18 March 1994.
- Folta, D., and D. Quinn (2006), Lunar frozen orbits, AIAA 2006-6749 paper presented at AAIA/AAS Astrodynamics Specialist Conference and Exhibit 21–24 August 2006, Keystone, Colo.
- Gehrels, T., T. Coffeen, and D. Owings (1964), Wavelength dependence of polarization. III. The lunar surface, *Astron. J.*, 69(10), 826–852.
- Gill, P. E., and W. Murray (1978), Algorithms for the solution of the nonlinear least-squares problem, *SIAM J. Numer. Anal.*, 15(5), 977–992, doi:10.1137/0715063.
- Hapke, B. (1973), Darkening of silicate rock powders by solar wind sputtering, *Moon*, 7(3–4), 342–355.
- Hapke, B. (1981), Bidirectional reflectance spectroscopy: 1. Theory, *J. Geophys. Res.*, 86(B4), 3039–3054, doi:10.1029/JB086iB04p03039.
- Hapke, B. (1999), Scattering and diffraction of light by particles in planetary regoliths, *J. Quant. Spectrosc. Radiat. Transfer*, 61(5), 565–581.
- Hapke, B. (2002), Bidirectional reflectance spectroscopy 5. The coherent backscatter opposition effect and anisotropic scattering, *Icarus*, 157(2), 523–534, doi:10.1006/icar.2002.6853.
- Hapke, B. (2008), Bidirectional reflectance spectroscopy 6. Effects of porosity, *Icarus*, 195(2), 918–926, doi:10.1016/j.icarus.2008.01.003.
- Hapke, B. (2012a), *Theory of Reflectance and Emittance Spectroscopy*, Cambridge Univ. Press, New York.
- Hapke, B. (2012b), Bidirectional reflectance spectroscopy 7: The single particle phase function hockey stick relation, *Icarus*, 221, 1079–1083, doi:10.1016/j.icarus.2012.10.022.
- Hapke, B., W. Cassidy, and E. Wells (1975), Effects of vapor-phase deposition processes on the optical, chemical, and magnetic properties of the lunar regolith, *Moon*, 13(1–3), 339–353.
- Hapke, B., B. Denevi, H. Sato, S. Braden, and M. Robinson (2012), The wavelength dependence of the lunar phase curve as seen by the Lunar Reconnaissance Orbiter Wide-Angle Camera, *J. Geophys. Res.*, 117, E00H15, doi:10.1029/2011JE003916.
- Haruyama, J., et al. (2008), Planned radiometrically calibrated and geometrically corrected products of lunar high-resolution Terrain Camera on SELENE, *Adv. Space Res.*, 42(2), 310–316, doi:10.1016/j.asr.2007.04.062.
- Haruyama, J., et al. (2012), Lunar global digital terrain model dataset produced from SELENE (Kaguya) Terrain Camera Stereo Observations, Abstract 1200 paper presented at 43rd Lunar and Planetary Science Conference, held March 19–23, 2012 at The Woodlands, Tex., doi:10.1029/2008GL035692.
- Helfenstein, P. (1986), Photometrically determined surface physical properties of terrains on Ganymede, *Lunar Planet. Sci.*, 28, 333–334.
- Helfenstein, P., and M. Shepard (1999), Submillimeter-scale topography of the lunar regolith, *Icarus*, 131, 107–131.
- Hillier, J. K., B. J. Buratti, and K. Hill (1999), Multispectral photometry of the Moon and absolute calibration of the Clementine UV/Vis camera, *Icarus*, 141(2), 205–225, doi:10.1006/icar.1999.6184.

- Isaacson, P. J., A. B. Sarbadhikari, C. M. Pieters, R. L. Klima, T. Hiroi, Y. Liu, and L. A. Taylor (2011), The lunar rock and mineral characterization consortium: Deconstruction and integrated mineralogical, petrologic, and spectroscopic analyses of mare basalts, *Meteorit. Planet. Sci.*, 46(2), 228–251, doi:10.1111/j.1945-5100.2010.01148.x.
- Johnson, J., et al. (2006), Spectrophotometric properties of materials observed by Pancam on the Mars Exploration Rovers: 1. Spirit, *J. Geophys. Res.*, 111, E02514, doi:10.1029/2005JE002494.
- Johnson, J. R., M. K. Shepard, W. M. Grundy, D. a. Paige, and E. J. Foote (2013), Spectrogoniometry and modeling of Martian and lunar analog samples and Apollo soils, *Icarus*, 223(1), 383–406, doi:10.1016/j.icarus.2012.12.004.
- Kamei, A., M. Kogachi, T. Mukai, and A. M. Nakamura (1999), Incident angle dependence of backscattered light by regolith layers, *Adv. Space Res.*, 23(7), 1205–1208.
- Kieffer, H. H., and T. C. Stone (2005), The spectral irradiance of the Moon, *Astron. J.*, 129(6), 2887–2901, doi:10.1086/430185.
- Kieffer, H. H., and R. L. Wildey (1996), Establishing the Moon as a spectral radiance standard, *J. Atmos. Oceanic Technol.*, 13(2), 360–375.
- Lawrence, S. J., and P. G. Lucey (2007), Radiative transfer mixing models of meteoritic assemblages, *J. Geophys. Res.*, 112, E07005, doi:10.1029/2006JE002765.
- Lucey, P., et al. (2006), Understanding the lunar surface and space-Moon interactions, *Rev. Mineral. Geochem.*, 60, 83–219, doi:10.2138/rmg.2006.60.2.
- Lucey, P. G. (1998), Model near-infrared optical constants of olivine and pyroxene as a function of iron content, *J. Geophys. Res.*, 103(E1), 1703–1713.
- Lucey, P. G., D. T. Blewett, and B. R. Hawke (1998), Mapping the FeO and TiO₂ content of the lunar surface with multispectral imagery, *J. Geophys. Res.*, 103(E2), 3679–3699.
- Lucey, P. G., D. T. Blewett, G. J. Taylor, and B. R. Hawke (2000), Imaging of lunar surface maturity, *J. Geophys. Res.*, 105(E8), 377–386.
- Mazarico, E., D. D. Rowlands, G. A. Neumann, D. E. Smith, M. H. Torrence, F. G. Lemoine, and M. T. Zuber (2011), Orbit determination of the lunar reconnaissance orbiter, *J. Geod.*, 86(3), 193–207, doi:10.1007/s00190-011-0509-4.
- McCord, T. B., and J. B. Adams (1973), Progress in remote optical analysis of lunar surface composition, *Moon*, 7(3–4), 453–474.
- McCord, T. B., and T. V. Johnson (1970), Lunar spectral reflectivity (0.30 to 2.50 microns) and implications for remote mineralogical analysis, *Science*, 169(3948), 855–858, doi:10.1126/science.169.3948.855.
- McCord, T. B., M. P. Charette, T. V. Johnson, L. A. Lebofsky, C. Pieters, and J. B. Adams (1972), Lunar spectral types, *J. Geophys. Res.*, 77, 1349–1359.
- McEwen, A., and E. Eliason (1998), Summary of radiometric calibration and photometric normalization steps for the Clementine UVVIS images, Abstract 1466 paper presented at 29th Annual Lunar and Planetary Science Conference, March 16–20, 1998, Houston, Tex.
- McEwen, A. S. (1991), Photometric functions for photoclinometry and other applications, *Icarus*, 92(2), 298–311.
- McEwen, A. S. (1996), A precise lunar photometric function, *Lunar Planet. Sci.*, 27, 841–842.
- McEwen, A. S., and M. S. Robinson (1997), Mapping of the Moon by Clementine, *Adv. Space Res.*, 19(10), 1523–1533, doi:10.1016/S0273-1177(97)00365-7.
- McGuire, A. F., and B. W. Hapke (1995), An experimental study of light scattering by large, irregular particles, *Icarus*, 113(1), 134–155.
- McKay, D. S., R. M. Fruland, and G. H. Heiken (1974), Grain size and the evolution of lunar soils, in *Proceedings of the 5th Lunar Science Conference, Houston, Texas, March 18–22, 1974*, pp. 887–906, Pergamon Press, Inc., New York.
- McKay, D. S., G. Heiken, A. Basu, and G. Blanford (1991), *Lunar Sourcebook*, Cambridge Univ. Press, New York.
- Minnaert, M. (1941), The reciprocity principle in lunar photometry, *Astrophys. J.*, 93, 403–410.
- Mishchenko, M., L. Travis, and A. Lacis (2002), *Scattering, Absorption, and Emission of Light by Small Particles*, Cambridge Univ. Press, New York.
- Mustard, J. F., and C. M. Pieters (1989), Photometric phase functions of common geologic minerals and applications to quantitative analysis of mineral mixture reflectance spectra, *J. Geophys. Res.*, 94(B10), 13,619–13,634.
- Näränen, J., S. Kaasalainen, J. Peltoniemi, S. Heikkilä, M. Granvik, and V. Saarinen (2004), Laboratory photometry of planetary regolith analogs II. Surface roughness and extremes of packing density, *Astron. Astrophys.*, 426, 1103–1109, doi:10.1051/0004-6361.
- Nicodemus, F. E. (1965), Directional reflectance and emissivity of an opaque surface, *Appl. Opt.*, 4(7), 767, doi:10.1364/AO.4.0000767.
- Ohtake, M., et al. (2010), Deriving the absolute reflectance of lunar surface using SELENE (Kaguya) multiband imager data, *Space Sci. Rev.*, 154, 57–77, doi:10.1007/s11214-010-9689-0.
- Piatek, J. L., B. W. Hapke, R. M. Nelson, W. D. Smythe, and A. S. Hale (2004), Scattering properties of planetary regolith analogs, *Icarus*, 171(2), 531–545, doi:10.1016/j.icarus.2004.05.019.
- Pieters, C. (1977), Characterization of lunar mare basalt types. II-Spectral classification of fresh mare craters, in *Proceedings of the 8th Lunar Science Conference, Houston, Texas, March 14–18, 1977*, pp. 1037–1048, Pergamon Press, Inc., New York.
- Pieters, C., and T. B. McCord (1976), Characterization of lunar mare basalt types. I - A remote sensing study using reflection spectroscopy of surface soils, in *Proceedings of the 7th Lunar Science Conference, Houston, Texas, March 15–19, 1976*, pp. 2677–2690, Pergamon Press, Inc., New York.
- Pieters, C. M. (1978), Mare basalt types on the front side of the Moon—A summary of spectral reflectance data, in *Proceedings of the 9th Lunar and Planetary Science Conference, Houston, Texas, March 13–17, 1978*, pp. 2825–2849, Pergamon Press, Inc., New York.
- Pieters, C. M., and P. A. J. Englert (1993), *Remote Geochemical Analysis, Elemental and Mineralogical Composition*, Cambridge Univ. Press, New York.
- Pieters, C. M., L. A. Taylor, S. K. Noble, L. P. Keller, B. Hapke, R. V. Morris, C. C. Allen, D. S. McKay, and S. Wentworth (2000), Space weathering on airless bodies: Resolving a mystery with lunar samples, *Meteorit. Planet. Sci.*, 35, 1101–1107.
- Robinson, M. S., and B. L. Jolliff (2002), Apollo 17 landing site: Topography, photometric corrections, and heterogeneity of the surrounding highland massifs, *J. Geophys. Res.*, 107(E11), 5110, doi:10.1029/2001JE001614.
- Robinson, M. S., et al. (2010), Lunar Reconnaissance Orbiter Camera (LROC) instrument overview, *Space Sci. Rev.*, 150(1), 81–124, doi:10.1007/s11214-010-9634-2.
- Robinson, M. S., B. W. Denevi, H. Sato, B. Hapke, and B. R. Hawke (2011), LROC WAC ultraviolet reflectance of the Moon, Abstract 1842 paper presented at 42nd Lunar and Planetary Science Conference, The Woodlands, Texas, March 7–11, 2011.
- Rosenburg, M. A., O. Aharonson, J. W. Head, M. A. Kreslavsky, E. Mazarico, G. A. Neumann, D. E. Smith, M. H. Torrence, and M. T. Zuber (2011), Global surface slopes and roughness of the Moon from the Lunar Orbiter Laser Altimeter, *J. Geophys. Res.*, 116, E02001, doi:10.1029/2010JE003716.
- Saiki, K., K. Saito, H. Okuno, A. Suzuki, Y. Yamanoi, N. Hirata, and R. Nakamura (2008), Estimation of the lunar reflectance by ground-based observation using a tunable liquid-crystal filter telescope, *Earth Planets Space*, 60, 417–424.

- Sato, H., B. W. Denevi, M. S. Robinson, B. W. Hapke, A. S. McEwen, and LROC Science Operation Team (2011), Photometric normalization of LROC WAC global color mosaic, Abstract 1974 paper presented at 42nd Lunar and Planetary Science Conference, held March 7–11, 2011 at The Woodlands, Tex.
- Sato, H., M. S. Robinson, P. Mahanti, and A. K. Boyd (2013), Temperature dependent spectral responsivity of the LROC WAC, Abstract 2412 paper presented at 44th Lunar and Planetary Science Conference, held March 18–22, 2013 in The Woodlands, Tex.
- Scholten, F., J. Oberst, K. D. Matz, T. Roatsch, M. Wählisch, E. J. Speyerer, and M. S. Robinson (2012), GLD100: The near-global lunar 100 m raster DTM from LROC WAC stereo image data, *J. Geophys. Res.*, 117, E00H17, doi:10.1029/2011JE003926.
- Shepard, M. K., and B. A. Campbell (1998), Shadows on a planetary surface and implications for photometric roughness, *Icarus*, 134(2), 279–291, doi:10.1006/icar.1998.5958.
- Shepard, M. K., and P. Helfenstein (2007), A test of the Hapke photometric model, *J. Geophys. Res.*, 112, E03001, doi:10.1029/2005JE002625.
- Shepard, M. K., and P. Helfenstein (2011), A laboratory study of the bidirectional reflectance from particulate samples, *Icarus*, 215(2), 526–533, doi:10.1016/j.icarus.2011.07.033.
- Shkuratov, Y. G., L. Starukhina, H. Hoffmann, and G. Arnold (1999), A model of spectral albedo of particulate surfaces: Implications for optical properties of the Moon, *Icarus*, 137(2), 235–246.
- Shkuratov, Y. G., D. G. Stankevich, D. V. Petrov, P. C. Pinet, A. M. Cord, Y. H. Daydou, and S. D. Chevrel (2005), Interpreting photometry of regolith-like surfaces with different topographies: Shadowing and multiple scattering, *Icarus*, 173(1), 3–15, doi:10.1016/j.icarus.2003.12.017.
- Souchon, A. L., P. C. Pinet, S. D. Chevrel, Y. H. Daydou, D. Baratoux, K. Kurita, M. K. Shepard, and P. Helfenstein (2011), An experimental study of Hapke's modeling of natural granular surface samples, *Icarus*, 215(1), 313–331, doi:10.1016/j.icarus.2011.06.023.
- Souchon, A. L., S. Besse, P. C. Pinet, S. D. Chevrel, Y. H. Daydou, J. L. Jossel, L. D'Uston, and J. Haruyama (2013), Local spectrophotometric properties of pyroclastic deposits at the Lavoisier lunar crater, *Icarus*, 225(1), 1–14, doi:10.1016/j.icarus.2013.03.004.
- Stamnes, K., S. C. Tsay, W. Wiscombe, and K. Jayaweera (1988), Numerically stable algorithm for discrete-ordinate-method radiative transfer in multiple scattering and emitting layered media, *Appl. Opt.*, 27(12), 2502–2509.
- Tooley, C. R., M. B. Houghton, R. S. Saylor, C. Peddie, D. F. Everett, C. L. Baker, and K. N. Safrdie (2010), Lunar reconnaissance orbiter mission and spacecraft design, *Space Sci. Rev.*, 150(1–4), 23–62, doi:10.1007/s11214-009-9624-4.
- Tran, T., M. Rosiek, R. A. Beyer, S. Mattson, E. Howington-Kraus, M. S. Robinson, B. A. Archinal, K. Edmundson, D. Harbour, E. Anderson, and LROC Science Operation Team (2010), Generating digital terrain models using LROC NAC images, paper presented at ASPRS/GaGIS 2010 Fall Specialty Conference, 15–19 Nov., 2010, Orlando, Fla.
- Velikodsky, Y. I., N. V. Opanasenko, L. A. Akimov, V. V. Korokhin, Y. G. Shkuratov, V. G. Kaydash, G. Videen, S. A. Ehgamberdiev, and N. E. Berdalieva (2011), New Earth-based absolute photometry of the Moon, *Icarus*, 214(1), 30–45, doi:10.1016/j.icarus.2011.04.021.
- Wagner, J. K., B. W. Hapke, and E. N. Wells (1987), Atlas of reflectance spectra of terrestrial, lunar, and meteoritic powders and frosts from 92 to 1800 nm, *Icarus*, 69(1), 14–28.
- Whitaker, E. A. (1972), Lunar color boundaries and their relationship to topographic features: A preliminary survey, *Moon*, 4(3–4), 348–355, doi:10.1007/BF00562002.
- Wildey, R. L. (1963), The Moon's photometric function, *Nature*, 200, 1056–1058.
- Wildey, R. L. (1977), A digital file of the lunar normal albedo, *Moon*, 16, 231–277.
- Wu, Y., S. Besse, J.-Y. Li, J.-P. Combe, Z. Wang, X. Zhou, and C. Wang (2013), Photometric correction and in-flight calibration of Chang'E-1 Interference Imaging Spectrometer (IIM) data, *Icarus*, 222(1), 283–295, doi:10.1016/j.icarus.2012.11.010.
- Yokota, Y., et al. (2011), Lunar photometric properties at wavelengths 0.5–1.6 μm acquired by SELENE Spectral Profiler and their dependency on local albedo and latitudinal zones, *Icarus*, 215(2), 639–660, doi:10.1016/j.icarus.2011.07.028.